Development of Protocols to Increase the Size Monodispersity and Surface Charge of Silica Nanoparticles for Use in Crystalline Colloidal Arrays

by

Daniel N. Maienshein

B.S., Chemistry, Grove City College, 2019

B.S., Mathematics, Grove City College, 2019

Submitted to the Graduate Faculty of

the Dietrich School of Arts and Sciences in partial fulfillment

of the requirements for the degree of

Master of Science

University of Pittsburgh

2021

UNIVERSITY OF PITTSBURGH

DIETRICH SCHOOL OF ARTS AND SCIENCES

This thesis was presented

by

Daniel N. Maienshein

It was defended on

June 1st, 2021

and approved by

Haitao Liu, Professor, Department of Chemistry

Sean Garrett-Roe, Associate Professor, Department of Chemistry

Thesis Advisor: Sanford Asher, Distinguished Professor, Department of Chemistry

Development of Protocols to Increase the Size Monodispersity and Surface Charge of Silica Nanoparticles for Use in Crystalline Colloidal Arrays

Daniel N. Maienshein, M.S.

University of Pittsburgh, 2021

Crystalline colloidal arrays (CCAs) are three-dimensional, non-close packed periodic structures formed from the self-assembly of charged colloidal particles suspended in solutions of low ionic strength. CCAs made from nanoparticles can be tailored to diffract ultraviolet (UV), visible, or infrared light, and thus can be used as optical components in Raman spectrometers. For example, using CCAs as wavelength selection devices has enabled the hyperspectral imaging of explosive-contaminated surfaces. However, the fabrication of CCAs which diffract UV light at wavelengths below 229 nm and which exhibit high diffraction efficiencies and narrow bandwidths has not yet been accomplished. Synthesis or post-synthesis processing techniques expected to improve CCA diffraction efficiencies and bandwidths include increasing particle size monodispersity, increasing surface charge, and decreasing particle diameter. In this thesis, a protocol is developed to improve the size monodispersity of 185 nm silica nanoparticles (NPs) from 10% to 6%, and that of 100 nm silica NPs from 15% to 11%. After slight modification, this protocol is expected to work for particles of smaller diameter as well. Additionally, a two-step surface functionalization of 100 nm silica NPs using (3-trihydroxysilyl)-1-propanesulfonic acid (THOPS) was carried out in various pH conditions with the goal of maximizing the surface charge. The failure to significantly increase the surface charge is discussed, and hypotheses are provided to explain this result. Finally, outlines of future experiments and directions are given.

Table of Contents

List of Tables

List of Figures

Preface

Thank you, Dr. Asher, for supporting me in my goals and for encouraging me to see my project through even during those times when my motivation was low. Thank you, Ivan, for showing me the ropes of photonic crystal fabrication and pushing me to become a more independent researcher. Thank you, Ryan, for getting me interested in the Asher group in the first place and for getting to work alongside you on the photoacoustic project. Thank you also to everyone else in the research group for always offering helpful advice. Thank you, Mom and Dad, for having supported my education in many ways so that I have made it to the place where I am now.

1.0 Introduction

This introductory chapter is for the purpose of motivating the spectroscopic techniques we use for explosive detection, describing one of the technologies we use to increase detection selectivity, and identifying current research objectives.

1.1 Deep Ultraviolet (DUV) Raman Spectroscopy

Many research efforts today are devoted to developing technology that could reliably and quickly detect explosives for the prevention of terrorist attacks.[1–4] These efforts can be classified according to whether they involve contact or non-contact methods. Between these two categories, non-contact methods do not require direct interaction with the explosive threat, and thus they have a higher probability of safe detection than contact methods do. Standoff detection is a subset of non-contact detection methods where the detector is removed from the threat by at least one meter,[4] though certain standoff techniques are effective even up to 45 meters.[5] Methods for standoff detection are numerous and include reflection, light detection and ranging, laser induced breakdown spectroscopy, Raman, coherent anti-Stokes Raman scattering, photoacoustic, and terahertz methods.[1]

Among all standoff detection techniques, deep ultraviolet (DUV) Raman spectroscopy enjoys particular advantages for the detection of explosives. (In this thesis, DUV Raman is defined as Raman spectroscopy employing excitation wavelengths ≤ 250 nm, in accordance with previous work done in our research group.[6] However, it is good to be aware that some authors consider all wavelengths ≤ 350 nm to be DUV wavelengths.[7,8]) The next few sections present the many advantages of DUV Raman and introduce a current, practical challenge for DUV Raman imaging.

1.1.1 Theory of Raman Spectroscopy

Raman spectroscopy is the study of the rotational or vibrational transitions of a chromophore which arise from the coupling of incident light with molecular motions that cause a change in polarizability. When an applied electric field $\vec{E}$ interacts with a molecule, it induces a dipole moment $\vec{\mu}_{\text{ind}}$. The strength of coupling between the components of $\vec{E}$ and $\vec{\mu}_{\text{ind}}$ are scalars which can be collected into a matrix called the polarizability tensor $\boldsymbol{a}$.

$$\vec{\mu}_{\text{ind}} = \boldsymbol{a}\,\vec{E}. \tag{1}$$

For Raman, a chromophore must undergo a change in polarizability along some normal coordinate $\vec{Q}$. As the polarizability oscillates along $\vec{Q}$, so does the strength of coupling between certain components of $\vec{E}$ and $\vec{\mu}_{\text{ind}}$. The variation in polarizability is described by the Raman polarizability tensor, defined as

$$(\alpha_R)_{\rho\,\sigma} = \frac{\partial(a_{\rho\,\sigma})}{\partial\vec{Q}} \tag{2}$$

For a purely vibronic transition (no rotation considered) from state $|I\rangle$ to state $|F\rangle$, the elements of $\boldsymbol{\alpha_R}$ are supplied by the following formula:

$$(\alpha_{R\rho\,\sigma})_{I\to F} = \sum_V \frac{\langle F|\mu_\rho|V\rangle\langle V|\mu_\sigma|I\rangle}{E_V - E_I - E_L - i\Gamma} + \frac{\langle F|\mu_\sigma|V\rangle\langle V|\mu_\rho|I\rangle}{E_V - E_F + E_L + i\Gamma} \tag{3}$$

Here, V is any vibronic state intermediate between $|I\rangle$ and $|F\rangle$, E_L is the energy of incident light, E_V, E_I, and E_F are the energies of intermediate, initial, and final vibronic states, Γ is the homogeneous linewidth, and μ_ρ and μ_σ are components of the dipole moment operator indexed by ρ and σ.

Equation 3 is due to Kramers, Heisenberg, and Dirac and is also known as the sum-over-states formula.[9] Knowing $\boldsymbol{\alpha_R}$, one can express the Raman cross section of the transition from $|I\rangle$ to $|F\rangle$, integrated over all 4π steradians, by

$$\sigma_{I\to F}(E_L) = K \cdot E_s^3 \cdot E_L \cdot \sum_\rho \sum_\sigma |(\alpha_{R\rho\,\sigma})_{I\to F}|^2 \tag{4}$$

where K is a collection of constants and E_s is the energy of light scattered off the sample. In Raman spectroscopy, molecular information is obtained by collecting light which is inelastically scattered off the sample. When light is shone on a sample, the majority of incident light is scattered elastically, an event called Rayleigh scattering. The rest of scattered light is scattered either at a lower (Stokes scattering) or a higher (anti-Stokes scattering) frequency than the incident light. The loss or gain in frequency relative to the excitation frequency is equal to the frequency of the molecular motion associated with the scattering event. Of main interest to Raman spectroscopists is Stokes scattering, since it is more intense than anti-Stokes scattering, and thus easier to detect.

1.1.2 Advantages of DUV Raman

For a Raman experiment, one can choose excitation wavelengths in the ultraviolet, visible, or infrared (IR) region. However, using DUV wavelengths has multiple advantages. One advantage is the dependence of Raman scattering intensity on the fourth power of the excitation frequency, which is made evident by the product of ${E_s}^3$ and E_L in Equation 4. This fourth-power dependence results in greater signal-to-noise ratios for Raman spectra produced using a DUV laser than for spectra generated by a visible or IR laser.[1,6] Another advantage is that fluorescence is not a significant source of interference in a DUV Raman experiment, unlike in visible Raman.[6]

For detecting explosives, there is also the very important advantage of resonance Raman enhancement. Resonance Raman (RR) is a special case of Raman spectroscopy where the excitation frequency lies within an electronic absorption band of a molecule, capable of leading to signals 10^6 times more intense than the case of non-resonance Raman.[10] Resonance enhancement can be predicted by considering Equation 3. As the energy of an incident photon approaches the the energy of a vibrational mode of the molecule, E_L approaches $E_V - E_I$. The result is that the (complex) absolute value of the denominator becomes very small, making the contribution of the first term in the sum very large. This makes the Raman polarizability element $(\alpha_{R\rho\sigma})_{I\to F}$ very large relative to other transitions. Therefore, by tuning the frequency (wavelength) of the incident light, one can selectively study Raman

bands of interest while preventing all the others bands from interfering with analysis.[9] Since the absorption maxima of most explosives occur below 260 nm,[4,11,12] DUV laser sources are required in order achieve RR enhancement for explosives, making DUV Raman especially appealing for explosive detection.

1.1.3 A Challenge for DUV Raman

One very useful form of Raman spectroscopy for explosive detection is wide-field hyperspectral imaging.[6,13] In this context, a hyperspectral image of a surface is one that associates a Raman spectrum to each position on the surface. A block diagram (excluding mirrors and lenses) is provided in Figure 1 to illustrate a hyperspectral imaging spectrometer. A laser outputs DUV light, and the beam is expanded to illuminate the entirety of a surface contaminated with explosive residue. Stokes-scattered light is then directed onto a wavelength selection device (WSD), which allows only a narrow range of wavelengths to pass, rejecting all the others. Light which meets the criterion for passage arrives at a charge-coupled device (CCD) camera, from which an image of the sample is reconstructed. Intense spots in the reconstructed image correspond to regions of the sample which strongly scatter light of the selected wavelengths. Dark regions correspond to parts of the sample which do not scatter or which scatter light that is rejected by the WSD. By tuning the wavelengths of light that are allowed to pass to the CCD via the WSD, a hyperspectral image of the sample can be constructed.

Although hyperspectral imaging is appealing due to the amount of information it can provide, there is a dearth of WSDs that are operational in the DUV. In fact, it was only in 2017 that the first DUV WSD was fabricated using a crystalline colloidal array (CCA), which is an optical device introduced in section 1.2.1. Hence, DUV WSD technology is still in its infancy, and there is much room left for optimization.[6] Since 2017, the Asher group has explored other materials for use as WSDs such as inverse opals (IOs), which are touted as being more mechanically, thermally, and photochemically stable than CCAs.[14] Despite these advantages, CCAs are still better than IOs in terms of optical performance[14] and ease of fabrication, since the assembly of high quality IOs relies upon mechanisms which are still

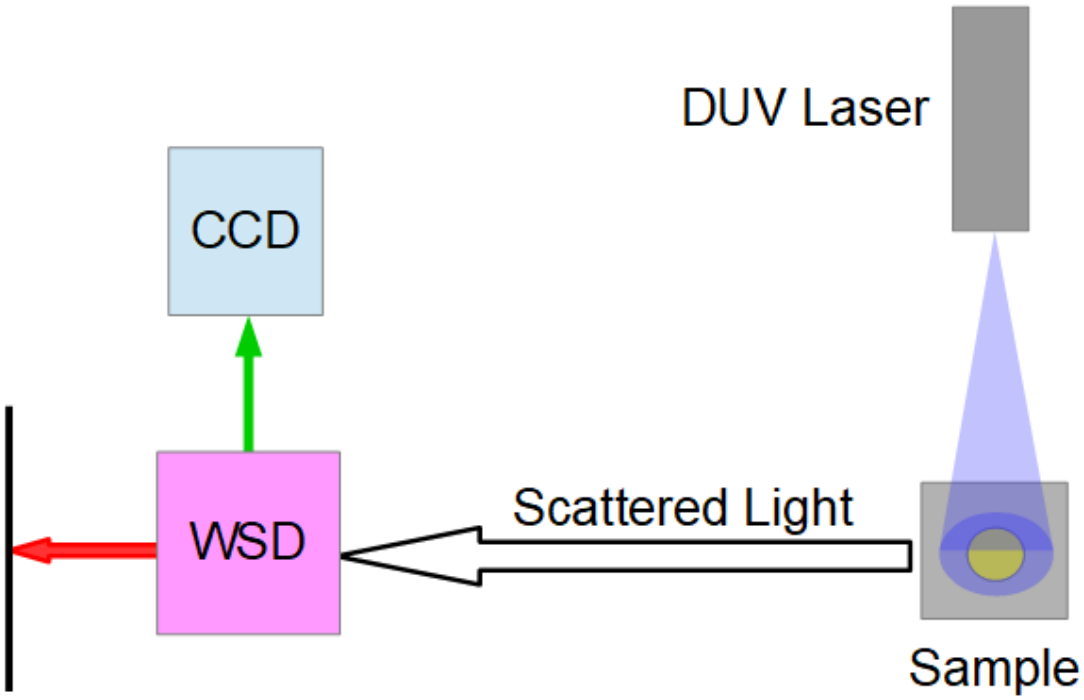

Figure 1: Block diagram of a wide-field hyperspectral imaging spectrometer. A DUV laser probes a large region of a surface containing explosive residue (yellow circle). The scattered light is directed onto the WSD, which allows only a narrow range of wavelengths (green arrow) to pass to the CCD, while rejecting all other wavelengths (red arrow).

not completely understood.[14–16] Thus, the development of improved CCAs for use as WSDs is a relevant and important challenge for DUV Raman.

1.2 Crystalline Colloidal Arrays (CCAs)

1.2.1 Definition and Comparison to Atomic Crystal Lattices

CCAs are type of material known as a photonic crystal (PhC). A PhC is any material with a periodic structure made from at least two components of differing dielectric constants.[17] The periodic structure of a PhC can be manifested in one, two, or three dimensions. A CCA is a three-dimensional photonic crystal formed from the self-assembly of non-close packed, charged colloidal particles suspended in solutions of low ionic strength.[18,19] The main driving force of CCA self-assembly is the achievement of a low energy face-centered cubic (FCC) or body-centered cubic (BCC) structure to minimize electrostatic interactions between like-charged particles. These crystal structures are stable due to long-range (around 1 µm) electrostatic interactions,[19,20] although the structures can be disturbed simply by tapping on them. Figure 2 depicts one unit cell of a CCA which has self-assembled into a FCC structure. Analogously to the case of atomic crystal lattices, mathematical planes intersecting sets of particles can be identified using Miller indices.[21] In Miller index terminology, the two yellow planes shown in Figure 2 are (111) planes.

Before discussing how the FCC or BCC structure of CCAs gives them wavelength selection ability, it will be useful to recall a subject perhaps more familiar to most chemists, which is that of X-ray crystallography. X-ray crystallography works on the principle of X-ray diffraction by the various planes of an atomic crystal lattice.[21] This diffraction is possible for two reasons. First, X-rays have the capability to interact with crystal planes, because the wavelength range of X-rays (0.01 to 10 nm) spans the order of magnitude of plane spacings in a crystal. Secondly, diffraction occurs, because some of the X-rays which scatter off the crystal planes constructively interfere. The condition for constructive interference is

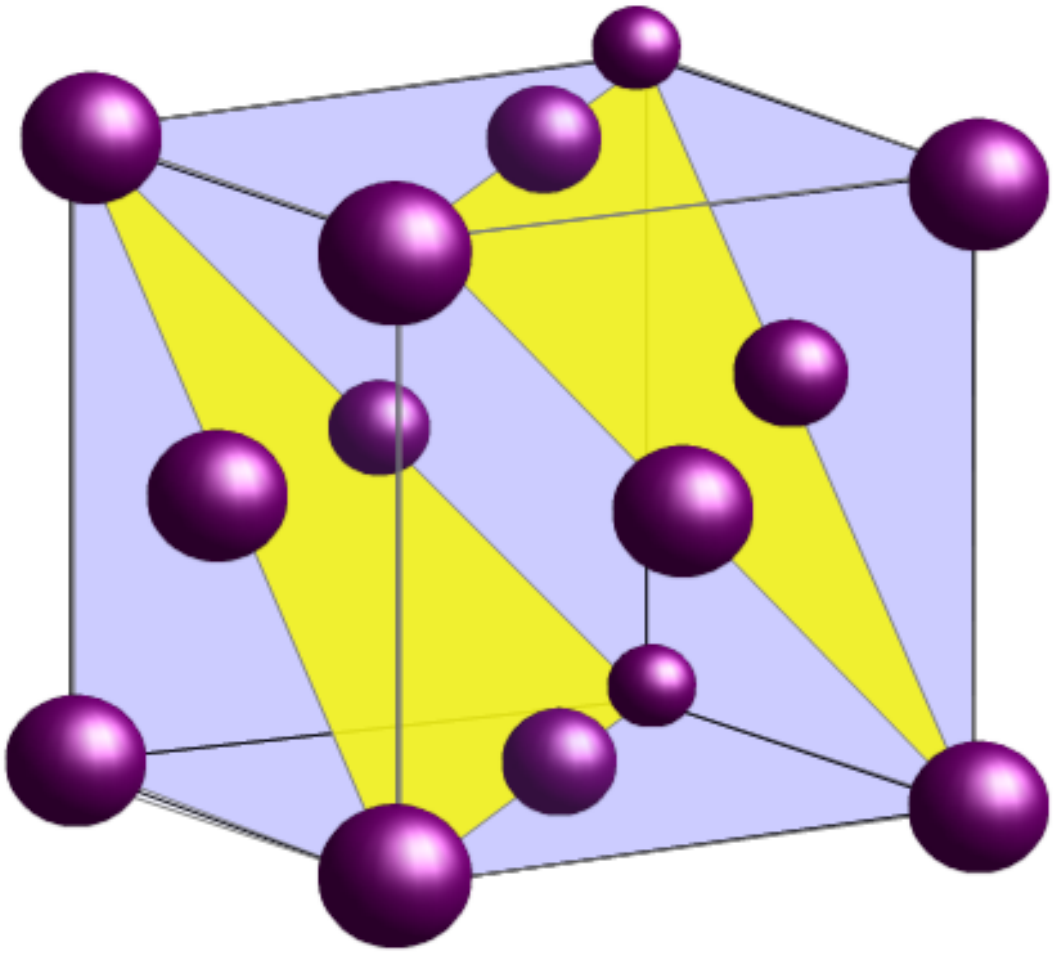

Figure 2: Unit cell of a non-close packed CCA.

described by Bragg's Law of diffraction.[19]

$$m\lambda = 2d\sin\theta \tag{5}$$

Here, m is the diffraction order, λ is the wavelength of the X-ray, d is the crystal plane spacing, and θ is the angle of incidence. A schematic of Bragg diffraction is shown in Figure 3.

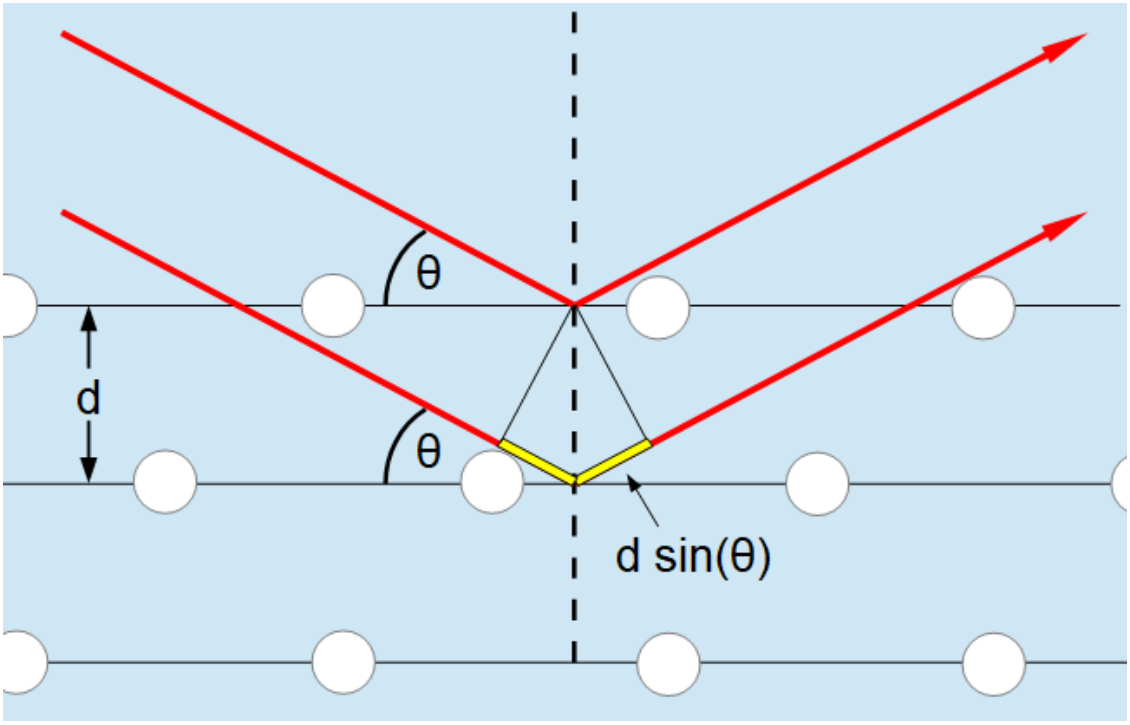

Figure 3: Bragg diffraction by an atomic crystal or CCA. Ordered atoms or nanoparticles are depicted as white circles. Incoming light rays (red) at angle of incidence θ interact with the periodic structure and constructively interfere when the Bragg condition is met.

1.2.2 CCAs for DUV Raman Spectroscopy

The major difference between CCAs and atomic crystals is size. Typical particle diameters and plane spacings found in CCAs are on the order of hundreds of nanometers, which is many orders of magnitude greater than atomic crystal plane spacings. Therefore, CCAs do

not diffract X-rays; rather, they diffract UV, visible, and IR light. Hence, CCAs constructed with the appropriate plane spacings can be used to redirect light of wavelengths relevant to DUV Raman spectroscopy (see Figure 4).

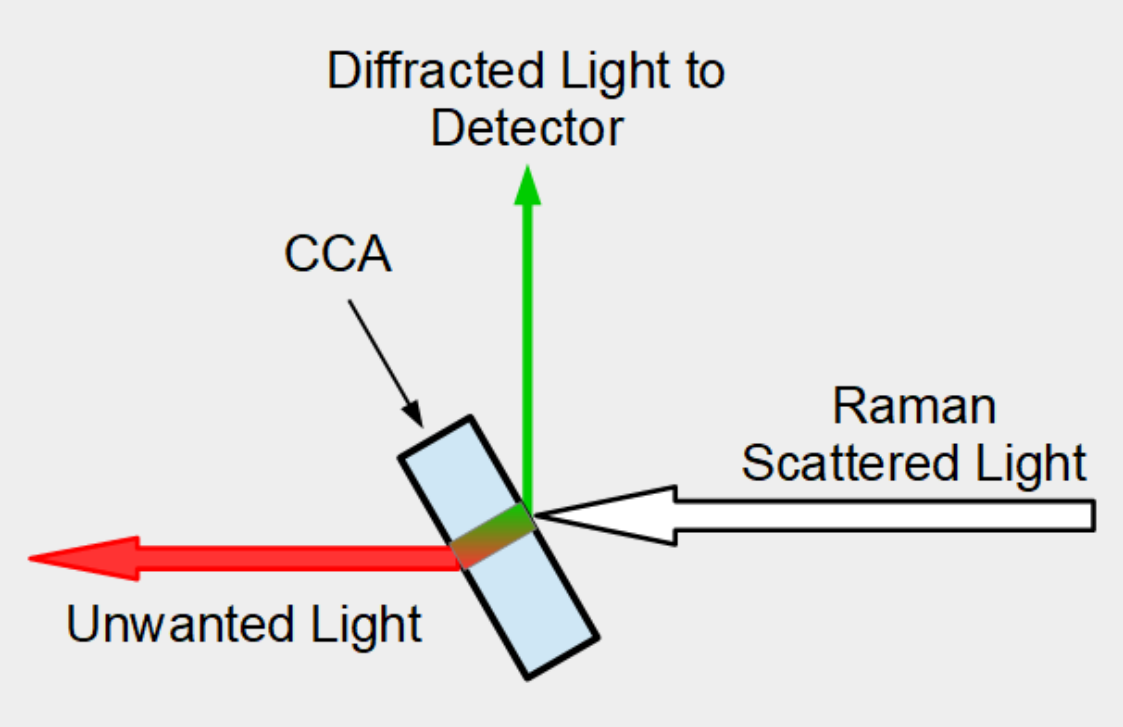

Figure 4: The role of a CCA in a Raman imaging spectrometer.

A range of wavelengths for which light propagation is forbidden through a CCA is called a stopband. In Figure 4, the red arrow represents light that is transmitted; these wavelengths do not belong to the stopband. On the other hand, the green arrow represents light that is Bragg-diffracted away from the crystal. Since these wavelengths cannot propagate through the crystal, they form the stopband. In theory, a stopband has zero width, because it is the exact wavelength $\lambda = 2d \sin\theta/m$, given by Bragg's Law (Equation 3). In reality, the stopband is broadened by such factors as incomplete CCA ordering, scattering of light off of the constituent particles, and imperfect collimation of incident light.[6] In spite of broadening, when designing a CCA for diffraction at a desired wavelength, one can use Bragg's Law as a rough guide to find the stopband center. Given a CCA made of suitable nanoparticle (NP) sizes, Bragg's Law predicts correctly that one can tune the angle of incidence or concentration

of the NP suspension (which alters the plane spacing) of the CCA to shift the stopband position.[22] In combination with real-life transmission scans, one can adjust the stopband center of a CCA very precisely. On the other hand, if a more accurate model is needed which also supplies the intensity and bandwidth of the stopband, more complicated formulations such as dynamical diffraction theory do exist.[23]

As a final note, CCAs usually have not one, but many potential stopbands, because there are many different Miller planes that can serve as the basis for Bragg diffraction. This abundance of diffracting planes would seem to pose a problem for WSDs, which work only if they diffract one narrow range of wavelengths at a time. Fortunately, the (111) planes are unique in that the wavelengths of light which they diffract at first order and close to normal incidence have no overlap with the wavelengths of light which are diffracted by the higher index Miller planes.[24] Thus, CCAs can be used as WSDs free of self-interference when the (111) planes are used.

1.2.3 Silica-Based CCAs

CCAs made for operation in the DUV must not absorb DUV light, or else major losses in optical throughput would result. Therefore, both the suspending medium and the material of which the NPs consist must be DUV-transparent. Polystyrene NPs are in some sense ideal for the construction of CCAs which are highly ordered, since they can be made very monodisperse (4% relative standard deviation) and highly charged (ζ-potential $\leq$ -81.8 mV at pH 5).[13] However, polystyrene admits absorption from 200 to 300 nm due its phenyl groups.[25] This absorption feature makes polystyrene particles unsuitable for DUV CCAs. On the other hand, silica (silicon dioxide, SiO_2) is DUV-transparent, making it a good candidate material for the fabrication of DUV CCAs. Indeed, the first CCA used as a DUV WSD mentioned previously was a silica-based CCA.[6]

1.2.4 The Structure of Silica NPs

In order to understand how silica particles become charged enough to form stable, diffracting crystals after self-assembly, it is first necessary to understand the structure of

silica NPs and their surface chemistry. The structure of silica is a covalent network, where each silicon atom is surrounded by four oxygen atoms in a tetrahedral arrangement.[26] This structure describes the usual arrangement of atoms and bonds on the interior of a silica NP. The network terminates at the silica surface, which is capped with hydroxyl groups.[27] Figure 5 depicts the interior and surface structure of a typical silica NP. In silica nomenclature, hydroxyl groups in conjunction with their underlying silicon atoms are called silanols, which are the silica chemistry analogues to alcohols. In Figure 5, an example silanol is circled in blue. Silicon and oxygen atoms which are bonded in the pattern Si-O-Si are called siloxanes, and these are analogous to ethers. Siloxanes are abundant both inside silica NPs and on their surfaces. A representative siloxane is circled in red.

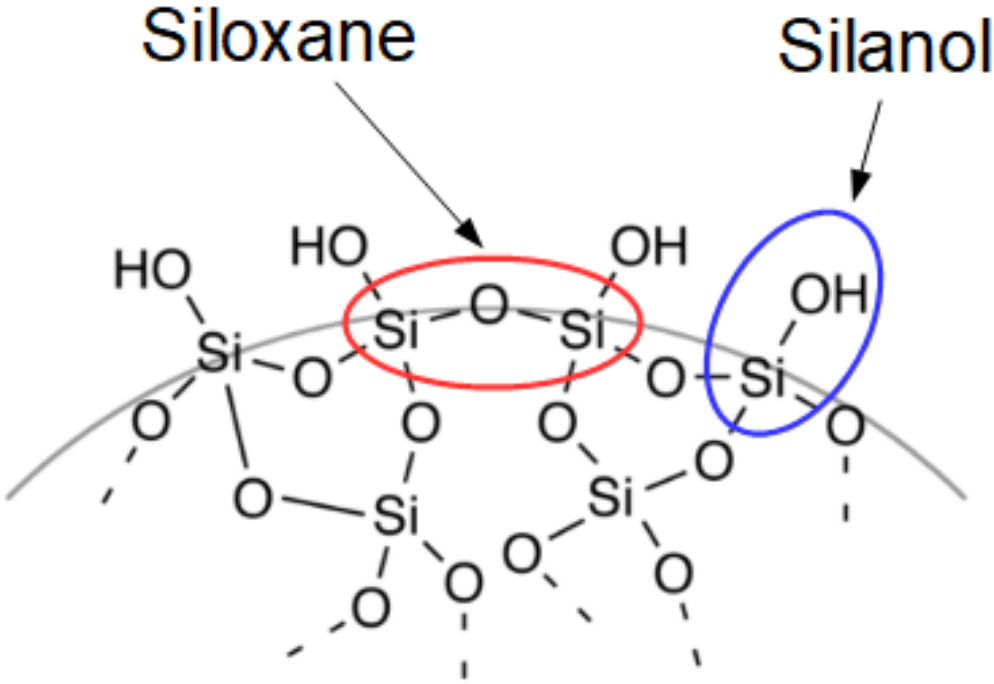

Figure 5: Internal and surface structure of a silica NP. Example siloxanes and silanols are identified. This figure was adapted from an original by Stéphane Mons. URL to figure: http://creativecommons.org/licenses/by-sa/3.0/, via Wikimedia Commons. Use of this figure is protected by CC BY-SA 3.0.

The average pKa of silanols on a silica NP surface is 6.8.[28] However, it is to be borne in

mind that this is only an average value, and pKas as a low as 2.1 and as high as 10.3 have been reported as a result of NP morphology and interactions between neighboring silanols.[26] These pKa values indicate that surface silanols on the whole are amphoteric, so that a fraction of them exist in a deprotonated state when suspended in pH 7 water. Due to these deprotonated silanols, silica NPs which have not been chemically altered do in fact have a measurable negative surface charge.[22] However, even in the absence of impurities which can screen electrostatic interactions, the amount of surface charge on non-functionalized NPs is not enough for self-assembly into stable CCAs.[22] Fortunately, surface silanols are reactive,[29–33] so that functional groups can be attached to a NP surface by reaction with them. If the attached groups are more ionizable in water than silanols, then the NPs can exhibit larger surface charges than the non-functionalized particle. Depending on the group attached, the surface charge can be made to be positive or negative. In either case, successfully-functionalized NPs possess a sufficient amount of surface charge to self-assemble into stable CCAs.[6,22] The next section will describe the reactions which enable functionalization of silica NPs.

1.2.5 Functionalization of Silica NPs with Trialkoxysilanes

In an aqueous environment, the two types of silanol reactions relevant to surface modification of silica NPs are condensation and hydrolysis.[28,34] Condensation is the reaction between two silanols, forming a siloxane bridge with concomitant loss of water; hydrolysis is the reverse process: the cleavage of a siloxane bond by water. Figure 6 shows the condensation and hydrolysis reactions of a silanol on the surface of a silica NP with another silanol.

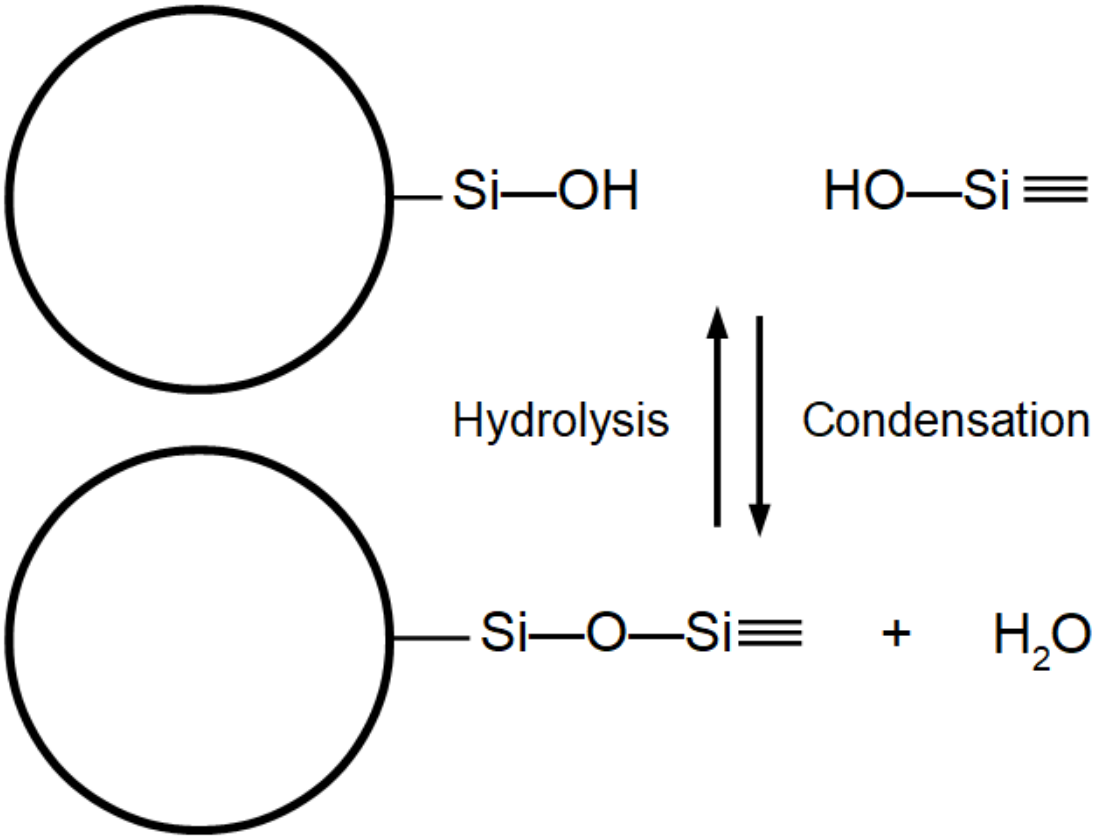

Figure 6: Hydrolysis and condensation of two silanols. A siloxane bridge is formed through condensation and is cleaved by hydrolysis.

In view of these reactions, functionalization of silica NPs in water can be accomplished through the condensation of surface silanols with trialkoxysilanes, which are molecules of the form $(RO)_3$-Si-X. In this formula, R represents H, Me, or Et, and X is an organic moiety which imparts the surface functionality desired. If R = Me or Et, then prior to condensation with a surface silanol, hydrolysis of OR to OH occurs in a quick first step.[35,36] Trialkoxysilanes come in a large variety, with functional groups ranging from basic amines[37,38] to long hydrocarbon chains[39] to acidic sulfonic acids.[22,32] Figure 7 shows the structure of a few trialkoxysilanes used in the literature: 3-(aminopropyl)triethoxysilane (APTES), dodecyltrimethoxysilane (DTMS), and 3-(trihydroxysilyl)-1-propanesulfonic acid (THOPS).

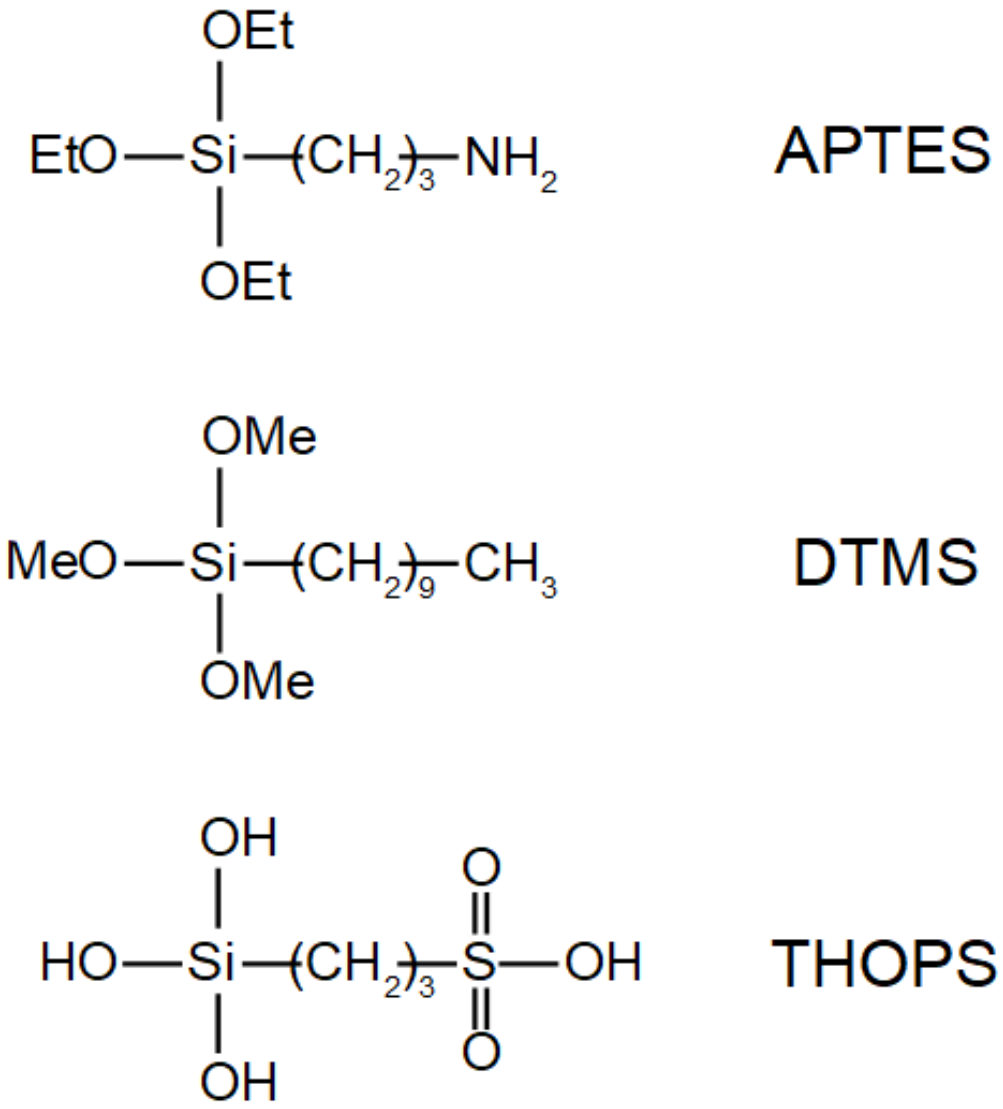

Figure 7: Examples of trialkoxysilanes used for functionalizing silica. Top: APTES; Middle: DTMS; Bottom: THOPS.

Our research group uses 3-(trihydroxysilyl)-1-propanesulfonic acid (THOPS) for functionalization of silica NPs used to fabricate CCAs.[6,22] While Rodriguez was the first to demonstrate the functionalization of silica NPs using THOPS in 2008,[32] our group pioneered the use of THOPS-functionalized NPs for making CCAs. The reason why THOPS is the ideal trialkoxysilane for our research is twofold. First, THOPS is transparent to DUV light.[6,22] Second, THOPS terminates in a strong sulfonic acid group, with pKa < 1.[22] Thus, not only a fraction, but virtually all of the attached THOPS ligands exist in a deprotonated

state in water. Therefore, attachment of THOPS imparts high levels of surface charge to silica NPs while maintaining DUV transparency. To the best of our knowledge, no other compound rivals THOPS in simultaneously possessing both of these characteristics.

1.3 Research Objectives

Improving the selectivity of Raman-based explosive detection devices is the guiding aim for the research directions pursued in this thesis. Detection selectivity depends upon spectral resolution, which itself depends upon the stopband width of the WSD. If the WSD is a CCA, then the stopband with depends upon particle ordering. Thus, if DUV CCA technology is to continue to be developed and used in Raman imaging spectrometers for explosive detection, then the research objective with highest priority is the improvement of NP ordering.[6] The goals which would have the greatest impact on improving particle ordering if achieved are increasing the size monodispersity and surface charge of silica NPs.[6,13]

Based on the abundance of literature[40–42] which demonstrates the ability of centrifugation to sort NPs by size, we hypothesized that we could use centrifugation to collect monodisperse fractions of THOPS-functionalized NPs and use them to make CCAs which order more quickly and maintain their order for longer periods of time. Chapter 2 is devoted to the exploration of this hypothesis.

It was also observed that a routine functionalization of silica NPs with THOPS led to a surface charge greater than had been previously attained in our group using the same procedure.[6,22] We believed this difference to be due to reaction pH. From this initial data point, and knowing that the kinetics of silica condensation and hydrolysis depend on pH,[28,34] we hypothesized that we could optimize the pH of reaction to increase the amount of THOPS added and thereby witness an increase in the surface charge. The study of the influence of reaction pH is documented in Chapter 3.

2.0 Increasing Silica Nanoparticle Monodispersity

Increasing the monodispersity of silica NPs can be divided into two types: synthetic methods and post-synthetic methods. Synthetic methods refer to the tailoring of synthetic conditions during the synthesis of silica NPs to yield a highly size monodisperse product. The Stöber synthesis of silica NPs in 1968 was a landmark publication, since it was the first in which reaction conditions were explored to optimize silica NP monodispersity.[43] Papers even as recent as 2019 report about the effect of reaction time and reactant concentration on silica NP monodispersity.[44] Important as the Stöber synthesis was, alternate routes to synthesizing monodisperse silica have also been developed. One synthesis uses a two-phase system for control of the reaction rate and L-arginine as a catalyst and particle stabilizer.[45]

However, given the wide variety of commercial suppliers of silica NPs with CCA-relevant diameters, we thought it more efficient for us to simply purchase batches of NPs to use for functionalization with THOPS. Hence, post-synthetic techniques to increase the size monodispersity of NPs are of more interest to us. Moreover, post-synthetic techniques would be effective in counteracting the slight increase in polydispersity of silica NPs witnessed after functionalization with THOPS (see Figure 22 in Appendix A). Post-synthetic NP separation techniques include size exclusion chromatography, electrophoretic techniques, size selective precipitation, and centrifugation.[46,47] We decided to use centrifugation for increasing the monodispersity of silica NPs, given its relative simplicity of implementation.[40,41,48,49]

2.1 Sedimentation by Centrifugation

Centrifugation can be used to separate particles based on size, shape, or density. In order to understand how separation is achieved and then applied to making NPs more monodisperse, this section details the theory and practice of sedimentation in a centrifuge.

2.1.1 The Physics of Sedimentation

Three forces act upon an isolated nanoparticle suspended in a medium: the buoyant force, the drag force, and the centrifugal force. These forces are illustrated in Figure 8.

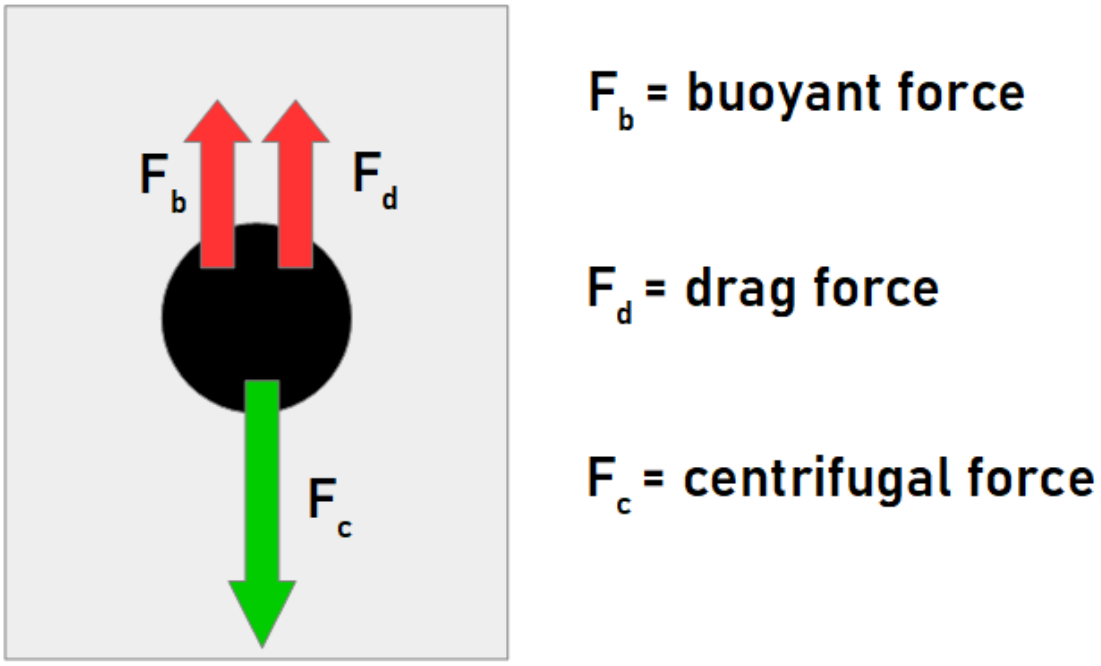

Figure 8: Free body diagram of a nanoparticle in a suspending medium and under the influence of a centrifugal force.

The buoyant force arises from the displacement of the surrounding medium by the nanoparticle. The equation for the buoyant force is given by: $F_b = -\frac{\rho}{\rho_p}\omega^2 rm$, where ρ is the density of the suspending medium in g/cm^3, ρ_p is the particle density in g/cm^3, ω is the angular velocity of the rotor with respect to the centrifuge rotor axis in s^{-1}, r is the radial distance of the particle from the rotor axis in cm, and m is the mass of a particle in g. Assuming spherically-shaped particles, m can be expressed in terms of the particle diameter and density.[50]

The drag force is due to frictional resistance as the particle moves through the medium. Assuming spherical particles, $F_d = 3\pi\eta dv$, where η is the viscosity of the suspending medium in poises, d is the hydrodynamic particle diameter in cm, and v is the particle velocity in cm s^{-1}. The hydrodynamic diameter of a particle is slightly larger than the "actual" hard

sphere diameter and is defined to be the distance between slipping planes on opposite sides of the particle. (The slipping plane defines a boundary between those ions in solution which move freely and those ions which are bound to the particle, moving with it as one unit.)

Finally, the centrifugal force is given by $F_c = m\omega^2 r$, where the symbols m, ω, and r have been defined above. By summing these three forces and setting the result to zero, one derives the terminal sedimentation velocity for a nanoparticle, which is sometimes called the Svedberg equation.

$$v = \frac{d^2(\rho_p - \rho)}{18\eta}\omega^2 r \tag{6}$$

2.1.2 Types of Centrifugal Separation Methods

Equation (6) suggests different ways to separate a mixture of spherical NPs in a centrifuge. For instance, since the sedimentation rate is proportional to the square of the diameter, then NPs differing with respect to diameter should be able to be separated. To carry out a size separation in practice, the most straightforward approach is called differential centrifugation (DC). DC (Figure 9, boxes A and D) is the separation of suspended NPs in a centrifuge by differences in sedimentation rate, where the suspension is evenly distributed throughout the entire centrifuge tube before centrifugation is begun. After centrifuging for a sufficient period of time, a pellet of tightly-packed NPs forms at the bottom of the tube. This pellet is primarily composed of larger particles in the suspension, since they sediment more quickly than smaller particles. Smaller particles primarily remain suspended in the supernate. However, small particles which are initially near the bottom of the tube reach the bottom very quickly. Thus, a fraction of the smaller particles contaminate the pellet. For this reason, it is common to perform multiple centrifugation runs in order to improve the pellet purity.[50]

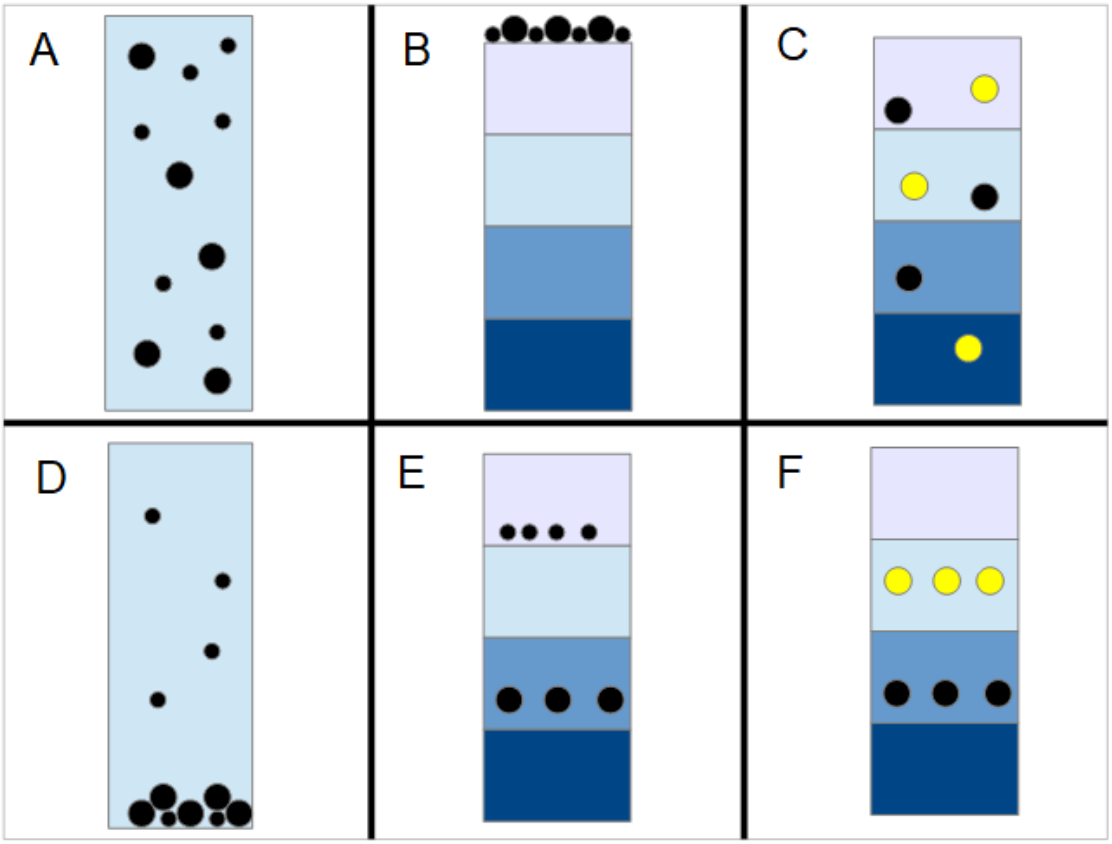

Figure 9: Illustration of the three types of centrifugation. A, B, and C: Initial state of particles to be separated by DC, RZC, and IZC, respectively. D, E, and F: Final state of particles after DC, RZC, and IZC, respectively. In boxes C and F, yellow particles have a lower density than black particles.

A modification to DC can be made that prevents cross-contamination of large particles with small particles altogether, allowing separation in one step. This method is referred to as rate-zonal centrifugation (RZC) (Figure 9, B and E). RZC is the separation of suspended particles in a centrifuge by differences in sedimentation rate, where the suspension is initially deposited as a thin layer floating on top of a density gradient. (In this context, a density gradient is a solution with a density that varies linearly or stepwise along the centrifuge tube height coordinate.) Particles, both large and small, begin sedimenting from the top of the tube. Therefore, it is (ideally) impossible for smaller particles to bypass larger particles, since smaller particles sediment slower. It is crucial that the particle density be greater than the maximum density of the gradient, or else the particles might come to rest prematurely.

RZC derives its name from the fact that particles of the same size form sedimenting bands, or "zones." After centrifugation, the particles of interest can be extracted from their zone via pipetting or more advanced techniques.[50] Although the initial particle position is the only theoretical difference between DC and RZC, a crucial practical difference is that a density gradient must be used for RZC. Figure 9, boxes B, C, E, and F all depict centrifuge tubes filled with density step gradients. The role of a density gradient in RZC is the suppression of convection currents in the medium, which are typically attributed to thermal fluctuations.[51] However, since thermal fluctuations should be small, we also think that convection currents might arise due to the difference in density between the sedimenting NPs and the medium. As the NP sediments, it leaves empty space in its wake, and the less-dense medium rushes upward to fill the void, establishing a current. In either case, convection causes mixing between particles of different sizes and is suppressed by use of a density gradient.[42,50] Disadvantages of RZC relative to DC include the additional requirement of a density gradient and lower processing efficiency.

One other common centrifugation method is isopycnic-zonal centrifugation (IZC) (Figure 3, C and F). IZC is the separation of components which differ in density, and like RZC, a density gradient is required. After sufficient centrifugation times, components come to rest at a position in the gradient with the same density. Thus, the density gradient in IZC plays a completely different role than it does in RZC and is not used to intentionally suppress convection. For IZC, the initial distribution of particles in the centrifuge tube is irrelevant, which makes IZC very straightforward to carry out. Despite the ease of IZC, it is inapplicable to the separation of silica NPs by size, since they all have the same density; thus either DC or RZC must be used for this study.

2.2 Implementation of Rate-Zonal Centrifugation for NP Separation

We chose to use RZC following the success of Hu and Chen in 2015 in isolating size-monodisperse fractions of 260 nm silica NPs. They showed that by increasing the monodispersity of NPs using RZC, they could decrease stopband widths and diffraction efficiencies

of closed-packed PhCs made from them. Bandwidths were decreased from 66 to 16 nm, and reflectivity values rose from 75% to 99%.[40] Inspired by this result, we developed a protocol in our lab to isolate monodisperse fractions of silica NPs. However, we initially could not reproduce the results of Hu and Chen, because they omitted many important procedural details in their paper. We became increasingly skeptical of their method when we determined that their calculated sedimentation rates were in error. Nevertheless, we ultimately succeeded in developing a functional and predictive protocol similar to theirs, which we used to achieve a reduction in polydispersity of 185 nm silica NPs from 9.7% to 5.6% and of 100 nm silica NPs from 15% to 11%.

2.2.1 The Importance of Rotor Choice

Initial attempts using our benchtop centrifuges for RZC of silica NPs failed due to unexpected broadening of sedimenting zones, incomplete separation of NPs by diameter, and the inability to model observed sedimentation rates via the Svedberg equation (Equation 6). These negative results led us to question our choice of centrifuge rotor. Our benchtop centrifuges are equipped with fixed-angle rotors, but another type of rotor is the swinging-bucket rotor.

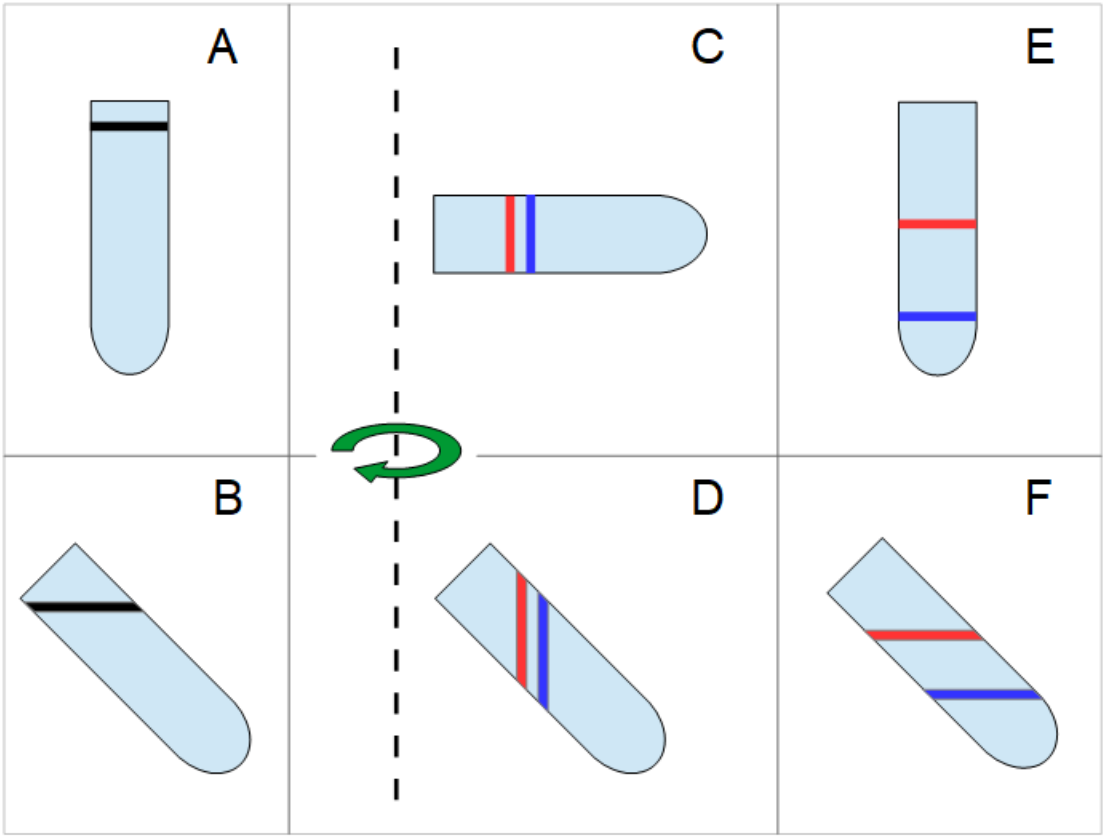

Figure 10: Comparison between RZC in a swinging-bucket rotor (boxes A, C, and E) and a fixed-angle rotor (boxes B, D, and F). A suspension containing two differently-sized particles, shown as black band, is placed on top of each centrifuge tube (A and B). During centrifugation (C and D), a centrifugal force is generated by the spinning rotor and is directed perpendicular to the axis. Separating bands in the swinging-bucket rotor (C) maintain their orientation relative to the centrifuge tube, while bands in the fixed-angle rotor (D) rotate 90 degrees with respect to the tube due to the centrifugal force. After centrifugation is complete (E and F), the separated bands return to a state of rest; in the case of the fixed-angle rotor, the bands must again reorient themselves with respect to the tube. Distortion and broadening of bands is not shown.

A literature search revealed that fixed-angle rotors are unsuitable for RZC,[42,48,52] while swinging-bucket rotors are suitable. In a swinging-bucket rotor, the centrifuge tube is placed in a bucket which is free to pivot. At rest, gravity is the dominant force, so the bucket is oriented upright. When the rotor is spinning, the centrifugal force is dominant, and since this force is oriented perpendicular to the rotor axis, the bucket swings out. Thus, the centrifuge tube is horizontal during centrifugation. In particular, sedimenting bands of

particles in a swinging-bucket rotor remain parallel to the rotor axis before, during, and after centrifugation. On the other hand, a fixed-angle rotor constrains the centrifuge tube to one specific angle with respect to the axis of rotation, so that when the rotor transitions from a state of rest to a state of spinning, the centrifuge tube cannot change orientation. However, the sedimenting bands inside the tube still rotate 90 degrees to align with the centrifugal force. This realignment with respect to the centrifuge tube can cause bands to become distorted and can lead to mixing of separating bands.[42] A visual comparison between the two rotor types is provided in Figure 10. Hu and Chen did not state which type of rotor they used in their NP separation.[40] However, due to our failure using a fixed-angle rotor and the theoretical superiority of swinging-bucket rotors for RZC, we adopted the use of a Sorvall TC7 centrifuge (Sorvall) equipped with a swinging bucket rotor (RTH-250).

2.2.2 An Improved Svedberg Equation

Before attempting to collect monodisperse fractions of silica NPs using the Sorvall, we wanted to ensure that we could model sedimentation rates using Equation 6. This equation is reprinted here for the reader's convenience.

$$v = \frac{d^2(\rho_p - \rho)}{18\eta}\omega^2 r$$

Modifications to this equation were made in order to maximize its predictive ability. Hu and Chen already recognized that, due to the gradient, the density ρ and viscosity η actually vary with particle displacement h in the centrifuge tube. However, they only calculated lower and upper bounds on sedimentation rates based on the lowest and highest densities and viscosities present.[40] Bounding the sedimentation rate avoids having to describe the step gradient with a piecewise function, which is necessary due to the discontinuities in density values. We chose to take the small extra step of defining the density in a piecewise manner in order to model sedimenting NPs as best we could.

The other variable that depends upon the particle displacement h is r, the radial distance from the rotor axis to the particle. As the particles continues to sediment, r increases. This variable r can be found via $r(h) = h + R$, where R is the distance from the axis of rotation to

the surface of the density gradient, which is a constant. Viewing the Svedberg equation as depending upon h, one obtains the displacement-dependent sedimentation velocity of NPs in a centrifuge tube:

$$v(h) = \frac{d^2(\rho_p - \rho(h))}{18\eta(h)}\omega^2 r(h) \tag{7}$$

2.3 Experimental

Silica NPs 185 nm in diameter were synthesized using the Stöber method.[43] NP samples for RZC were prepared by loading either a 200 or 350 µL aliqout of 13% (w/v) 185 nm silica NP suspension on top of a sucrose density step gradient in a 15-mL conical centrifuge tube. Loading volumes and NP wt% values were selected in accordance with the optimal ranges for these parameters found by Hu and Chen.[40] For sedimentation rate experiments, 200 µL was used, while for collection of monodisperse fractions, 350 µL was used. The step gradient was composed of layers of sucrose with the following concentrations (listed in order from top to bottom of the tube): 250, 350, 400, and 510 mg/mL. Each layer was made to be 1 cm thick. The step gradient was prepared only minutes before use to prevent mixing of layers due to diffusion. Gradient stock solutions were stored in a refrigerator at 4°C when not in use. Nanoparticles were layered on top of the gradients only one minute before the start of centrifugation to prevent premature sedimentation.

Two samples were prepared as above for tracking the observed sedimentation rate for comparison with the rate predicted by Equation 7. The NPs were centrifuged for a total of 40 minutes in the Sorvall at 3200 revolutions per minute (RPM) and 25 °C. The rotor brake was enabled, which decelerates the rotor from full speed to 200 RPM before coming to rest freely. It was observed that the NP suspension separated into an upper, more concentrated band, and a lower band, less concentrated band. A pellet also formed at the bottom of the tube during centrifugation. Figure 11 shows the distribution of the sedimenting NPs after 10 minutes in the centrifuge. The lower, less visible band is attributed to agglomerates of two or three particles which formed during sedimentation, and the pellet is attributed to

larger agglomerates which precipitated very quickly to the bottom due to their large collective diameter. The upper, more concentrated band, believed to be composed of individual unagglomerated particles, was the band that was tracked for modelling of sedimentation rates and the extraction of monodisperse fractions.

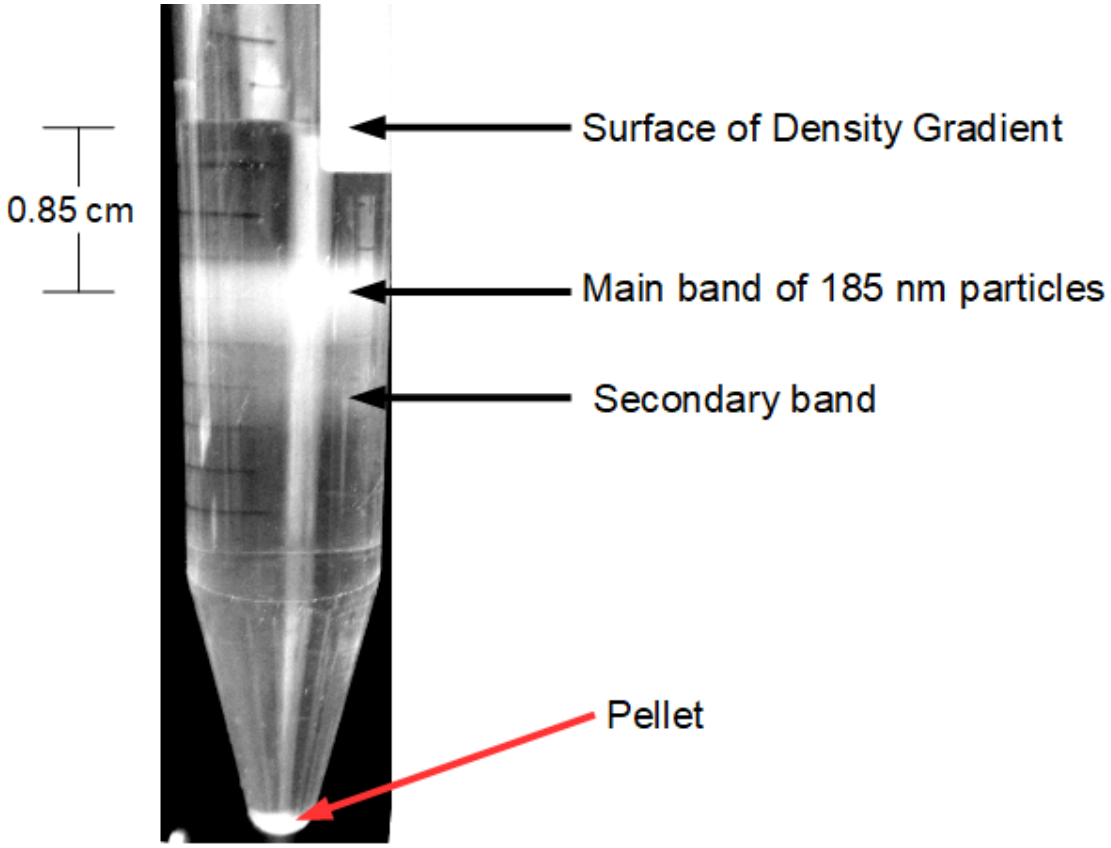

Figure 11: Photograph of a sedimenting band of 185 nm non-functionalized silica NPs. This photo was taken after centrifugation for 10 minutes at 1330 x g in a Sorvall TC7 centrifuge equipped with a swinging bucket rotor (RTH-250). Chamber Temperature: 25°**C.**

Positions and widths of the upper band were recorded every 10 minutes by marking them directly on the the centrifuge tube and measuring them to millimeter precision with a ruler. Then, the particle displacement was plotted against time on the same graph as the theoretical displacement, which is shown in Figure 12. Refer to Appendix C for the calculation of the theoretical sedimentation rate vs time.

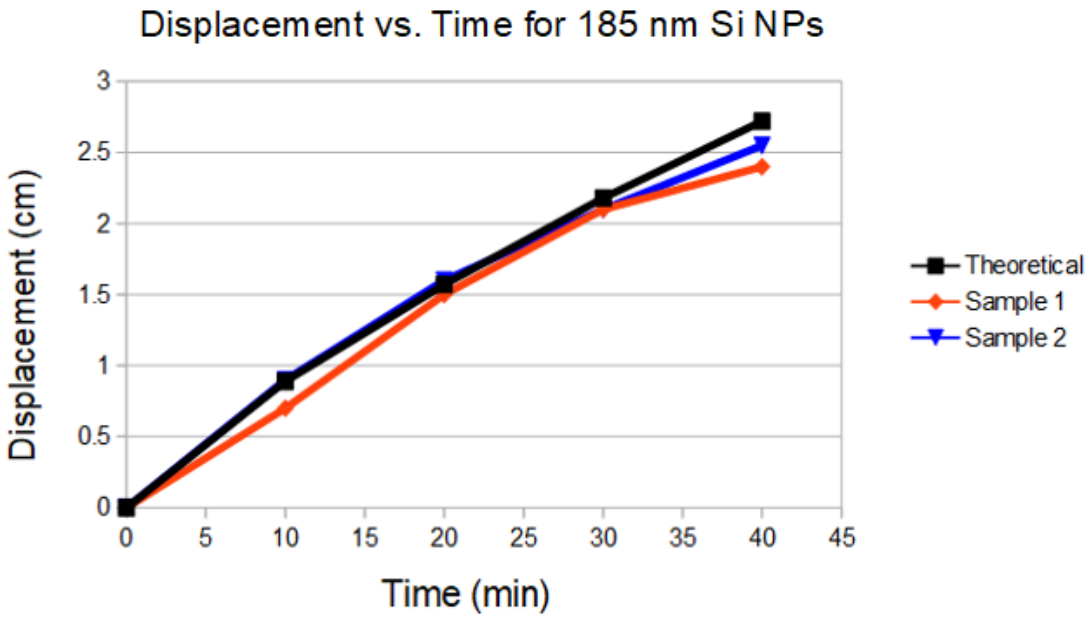

Figure 12: Sedimentation of 185 nm silica NPs at 3200 RPM (rcf = 1465 × g at the top of the centrifuge tube). Instrument: Sorvall TC7 centrifuge equipped with a swinging bucket rotor (RTH-250); Chamber Temperature: 25°C; Density gradient steps: 250, 350, 400, and 510 mg/mL, each 1 cm thick.

Assuming that the upper band contained only unagglomerated, 185 nm particles, we performed another round of RZC in order to collect monodisperse fractions from this band. The fractionation experiment was set up in the same way as the rate experiment, except that 350 µL of NP suspension was layered on top of the step gradient. Centrifugation was stopped after 10 minutes for extraction of NPs. Figure 11 shows the state of NP sedimentation at the end of the centrifugation experiment. Particles were extracted by pipette from the upper band, which was located 0.85 cm below the density gradient surface. During collection, the pipette tip was swirled in a gentle, circular manner in order to fairly sample the entire band. For each sample, three 166 µL aliqouts were extracted from the band. Then, the sucrose was removed from the particles by washing them with water three times using an Eppendorf 5424 microcentrifuge with fixed angle rotor. Particles from each aliqout were redispersed in a total of 166 µL ethanol. One drop of each aliqout was dried on a Formvar-coated copper grid for sizing via transmission electron microscopy (TEM).

Table 1: Size distribution of 185 and 100 nm silica NPs before and after RZC

Before RZC	185 ± 18 nm	100 ± 15 nm
After RZC, Sample 1	188 ± 10 nm	101 ± 11 nm
After RZC, Sample 2	188 ± 11 nm	103 ± 11 nm

2.4 Results and Discussion

TEM images of 185 nm silica NPs before and after RZC were taken with a FEI Morgagni transmission electron microscope and analyzed to obtain particle size distributions. Representative images are included in Appendix A as Figures 23 and 24. Over 500 particles were analyzed in each case to ensure statistical confidence. The results summarized in Table 1 show that 185 nm silica NPs extracted from the upper band of a RZC experiment have a narrower size distribution than the original batch of particles. Overall, particle polydispersity was lowered from 9.7% to 5.6%, which is a drop of 4.1%. It is interesting to note that the mean particle diameter for both samples after RZC increased by 3 nm from the mean diameter of particles before RZC. Although the origin of this shift is uncertain, it should have little impact on the performance of CCAs, since it is only a 2% increase. In order to confirm the applicability of the RZC method to particles of smaller diameter, we also performed RZC on two samples of 100 nm silica NPs purchased from Superior Silica, LLC (SupSil Premium, 5 wt% in ethanol; abbreviation: SS100). A significant decrease in polydispersity was also seen for these particles, which is recorded in Table 1.

These results strongly suggest that particles of diameters $\leq$ 50 nm, used in the fabrication of DUV-diffracting CCAs,[6,22] could also be made more monodisperse using RZC. However, there are two main challenges for the centrifugation of smaller particles. First, since the sedimentation rate decreases with the square of particle diameter, either centrifugation times need to be increased, or higher rotors speeds need to be employed. Increasing centrifugation times is to be avoided on the grounds of processing inefficiency and diffusion of NPs. Thus, increasing the rotor speed is a natural path forward. Unfortunately, the

maximum speed for the safe operation of the RTH-250 rotor which we used is 3200 RPM, which corresponds roughly to 1330 x g. The use of an ultracentrifuge capable of obtaining centrifugal forces up to 1000000 x g would solve this problem. The second challenge for the separation of smaller particles is that their sedimenting bands are invisible. Although 185 and 100 nm particles are sufficiently large to scatter light even when fairly dilute, particles on order of 50 nm scatter significantly less intensely in the visible region, which makes the location of sedimenting bands by eye infeasible. To overcome this problem, the use of an ultracentrifuge equipped with a light absorption detector could be used to track sedimenting bands rather than tracking by eye.[53] In summary, we have demonstrated a significant increase in monodispersity of 185 and 100 nm silica NPs using RZC in an ordinary centrifuge. Additionally, there is much potential for the successful separation of smaller diameter silica NPs if an ultracentrifuge equipped with a light absorption detector were employed.

3.0 Synthesis of Highly-Charged Silica Nanoparticles

In this chapter, background information relating to functionalization of silica NPs is presented, followed by a study on the effect of reaction pH on the addition of silica NPs with THOPS. Hypotheses concerning the observed pH-independence of THOPS addition are presented, and future experiments and directions are suggested.

3.1 Background

3.1.1 Adsorption and Grafting Modes of Trialkoxysilanes

The goal of this first section is to make precise what is meant by the "amount" of trialkoxysilane such as THOPS that is "added" to a NP surface. It is important to recognize from the outset that there are multiple possible modes of addition.[54,55] Various modes of attachment are shown in Figure 13. The weakest form of addition is adsorption of the silane to the NP surface via van der Waals interactions such as hydrogen bonding. Molecules adsorbed to the surface are completely removed after several particle washing steps; thus adsorption is not a desirable mode of attachment.[55] What one usually seeks is the formation of a strong, covalent bond between the silane and the silica NP surface. This is referred to as grafting in the literature. Grafting occurs via a condensation reaction between the trialkoxysilane and the silanols on the silica NPs surface. Two kinds of grafting can occur, depending on the silane used in the synthesis and the reaction conditions. If trialkoxysilanes condense with each other prior to grafting, then a polymeric network covering the NP surface results.[29,35] On the other hand, if the trialkoxysilane is not self-reactive, then individual grafting results due to the formation of one to three siloxane bonds between the surface silanols and the trialkoxysilane. One and two bonds are commonly formed, but the formation of three bonds is believed not to occur in most instances.[29]

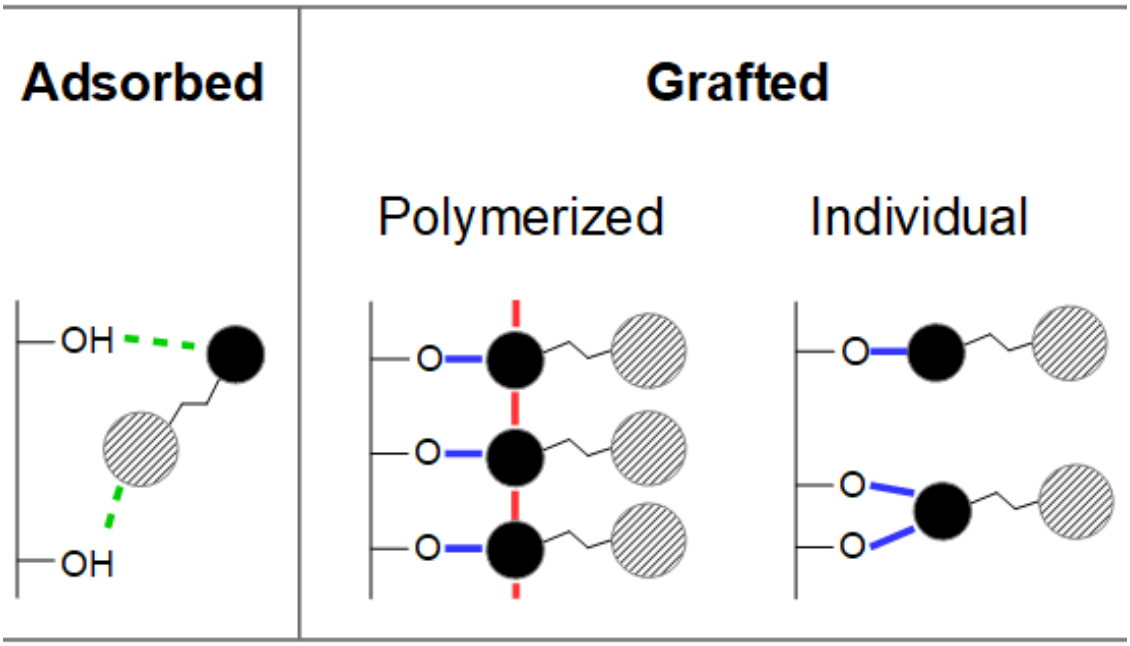

Figure 13: The modes of trialkoxysilane addition to a silica NP surface. Solid black circles represent the silanol functionality of the trialkoxysilane which participates in condensation, while hatched circles represent a functional group such as a sulfonic acid. Hydrogen bonds are shown as green dashed lines, covalent bonds between the trialkoxysilane and the NP surface as solid blue lines, and covalent bonds between two trialkoxysilanes as solid red lines.

In order to maximize the surface charge of silica NPs for use in CCAs, it is necessary to maximize the amount of THOPS grafted onto their surface. The value used to quantify the amount of silane grafted to a NP surface is called grafting density.[29–31,33,38,39] Grafting density is defined as the ratio of grafted silanes to the surface area of the NP. Grafting density can be expressed in various units, such as molecules nm^{-2} or $\mu mol\, g^{-1}$, where conversion between units is possible if the NP specific surface area (SSA), i.e., the surface area per gram, is known. In many cases, the SSA is provided by the NP manufacturer. If not, it can be measured experimentally.[31,33,39] For reference, 100 nm silica particles that we have purchased have SSAs between 40 and 50 $m^2\, g^{-1}$, while 50 nm particles from the same supplier have SSAs between 200 to 250 $m^2\, g^{-1}$.

3.1.2 Ways to Increase the Grafting Density of Trialkoxysilanes

Numerous studies have shown how reaction conditions can be tailored to increase the grafting density of trialkoxysilanes onto silica surfaces. The most straightforward approach is to increase the concentration of trialkoxysilane present in the reaction, as is demonstrated by multiple studies, including one specifically devoted to grafting of THOPS onto silica NPs. However, in every case the resulting grafting density levels off beyond a certain concentration of added silane.[22,36,39,54] Another approach to achieving higher grafting densities is to first ensure that the silica substrate is fully activated. In one study, the grafting density of a molecule similar to THOPS was increased by the addition of small quantities of NaCl to the water solvent.[56] The authors claim that the added salt promoted the transformation of surface siloxanes to reactive silanols through favorable ionic interactions. Other authors report that siloxanes failed to become activated by submitting silica surfaces to boiling or strong acids prior to grafting.[27] Finally, the role of reaction solvent has also been explored. For instance, using toluene as the reaction solvent led to lower grafting densities than water due to its inability to promote the hydrolysis of inactive siloxanes to reactive silanols.[56] A different study showed that toluene was twice as effective as ethanol in the grafting of APTES (structure in Figure 7) onto silica NPs.[57] It was concluded that the nonpolar nature of toluene limited the possible reactions of APTES only to those which could occur near the NP surface; in polar ethanol, competing interactions with the solvent and reactions with other APTES molecules could occur freely.

3.2 Study on the Effect of pH on THOPS Grafting Density

We chose to investigate a reaction condition other than those listed above. To the best of our knowledge, there has been only one study on the influence of reaction pH on the grafting density of trialkoxysilanes onto silica NPs. In this study, a trialkoxysilane was grafted onto 30 nm silica NPs in both acidic (pH 2.6) and basic (pH 9.9) conditions, and higher grafting densities were witnessed at the lower pH value.[36] Recently, our lab

also noticed a similar trend. We had purchased monodisperse, 50 nm diameter silica NPs (NanoCym, 5wt% in water) and then performed a routine functionalization of them with THOPS. After purification steps, it was observed that these THOPS-functionalized particles were more charged than we had expected, showing a ζ-potential of -84 mV at pH 4.5. Previous ζ-potentials measured in our lab for THOPS-functionalized silica NPs were much lower (-43 mV at pH 4 for 47 nm NPs[22] and -50.5 mV at pH 4.5 for 36 nm NPs[6]).

In order to determine the source of our fortuitous success, we compared the reaction conditions between our recent reaction and the older reactions. It was found that all reaction conditions were the same except for the reaction pH. In both older procedures, silica particles were synthesized in the presence of basic catalysts such as ammonia or L-arginine and functionalized without washing away these catalysts. Thus, these THOPS-functionalization reactions were run in basic conditions.[6,22] In contrast, no base was present in our more recent THOPS-functionalization reaction; we used pre-synthesized particles which were suspended in neutral water and ran the functionalization reaction in pH 4.5 nanopure water (18 MΩ cm).

We wondered whether we could confirm that pH plays a role in grafting density of THOPS and then leverage that dependence to increase the surface charge of our NPs. However, the authors who showed that pH can influence grafting density also witnessed significant particle agglomeration.[36] Although we never have witnessed particle agglomeration during THOPS-functionalization of silica NPs in our own lab, we wished to eliminate the possibility of agglomeration completely when systematically varying the reaction pH.[22,28,34] Therefore, we envisioned the following two-step approach to functionalize the silica NPs. In the first step, we would perform a routine THOPS-functionalization of silica NPs in order to protect them from agglomeration through electrostatic stabilization. Next, we would perform a second round of THOPS functionalization in pH 1, pH 4, and pH 7 conditions. Finally, the increase in grafting densities as a function of pH would be measured by ζ-potential and conductometric titration.

3.3 Experimental

3.3.1 Control Experiments

Control experiments were performed to test NP stability in solutions of varying pH values. Solutions were prepared with pH values of 1 (HCl / KCl), 4 (citric acid / KOH), and 7 (KH_2PO_4 / KOH). Then, a spare batch of 100 nm THOPS-functionalized silica NPs (NC100-THOPS) were dispersed in the pH 1, 4, and 7 solutions and were monitored over time by dynamic light scattering (DLS) at room temperature. Over the course of three days, DLS showed no sign of aggregation for all three solutions, as is shown in Figure 14. We also used DLS to monitor the particles dispersed in pH 4.5 water subjected to elevated temperatures (80 °C) which are used in the THOPS-functionalization reaction. We found that particles did not aggregate at elevated temperatures either. Finally, in addition to the DLS results, there was no visible sign of aggregation in any sample.

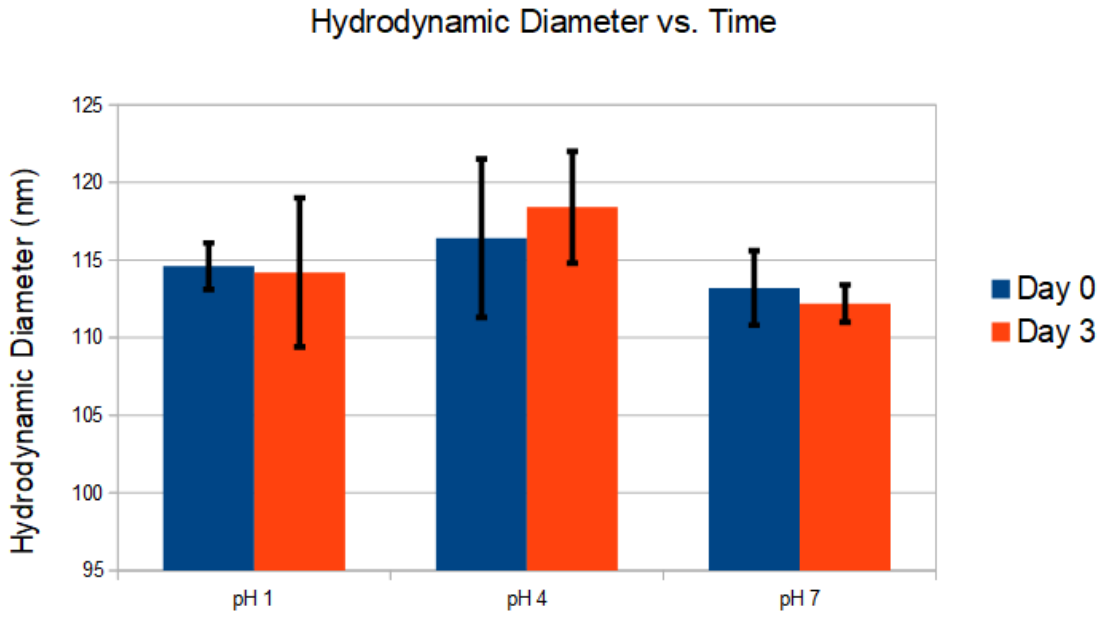

Figure 14: Hydrodynamic diameter of 100 nm silica-THOPS particles monitored by DLS at room temperature over the course of three days. It is evident that particles do not aggregate even in low pH environments, which is attributed to the fact that they are electrostatically stabilized by THOPS.

Table 2: Control experiment testing the change in pH of the reaction solution upon addition of THOPS with and without neutralization

pH without THOPS	pH with THOPS	pH with neutralized THOPS
0.95	0.8	1.02
3.98	3.8	4
7.01	6.5	6.98

Addition of THOPS presented an issue separate from aggregation, which warranted one more control experiment. Since THOPS is highly acidic, we wanted to ensure that we could maintain a constant pH during the reaction even after addition of THOPS. Since the actual reaction was to use 1 mL of THOPS (33.4% in water) per 100 mL of solution, we added 50 µL of THOPS to 5 mL of each solution (pH 1, 4, and 7). We also added 50 µL of THOPS that was neutralized ahead of time with KOH to 5 mL of each solution. The solution pH before and after addition of THOPS was monitored using a pH probe, and the results are summarized in Table 2. The pH of each solution decreased by an average value of 0.3 upon addition of THOPS which had not been neutralized, whereas the pH of each solution was maintained upon addition of THOPS which had been neutralized with KOH.

3.3.2 Initial Functionalization of 100 nm Silica Particles

Monodisperse SS100 NPs were functionalized with THOPS according to the standard procedure used in our lab and the literature.[6,22,32] The silica NPs were sonicated for forty minutes in their storage bottle prior to functionalization to ensure full de-agglomeration. Meanwhile, a Kontes 500-mL flask was immersed in a well-mixed oil bath, which was heated to a set temperature of 79.5 °C. A water-cooled condenser was attached to the middle neck of the flask. The sonicated NPs were added to the flask and diluted with 100 mL of nanopure water. A magnetic stir bar (Fisher, egg-shaped 1.25 by 0.62 inches) was added to the flask, and stirring at 140 RPM was begun. Finally, 4 mL of THOPS (which is in stoichiometric

excess) was neutralized by the addition of 800 µL of ammonium hydroxide. In doing so, the THOPS-NH_4OH solution acquired a yellow tint, which is most likely due to the presence of trace organic material from the plastic bottle in which the ammonia solution was stored. Once the solution temperature had equilibrated to 70 °C, the THOPS-NH_4OH solution was added dropwise to the reactor. The reaction was run for 6 hours.

After the reaction was complete, the particles were washed with water six times by centrifugation for one hour at 10000×g. The resistivity of the sixth supernate was 110 Ω cm, indicating successful removal of ions. The particles were then re-dispersed in a total of 50 mL of nanopure water (pH 4.5) and filtered through boiled glass wool into a clean bottle. Ion exchange resin (BioRad, AG® 501-X8) was added to the bottle to remove any remaining ions in solution. After cleaning, a ζ-potential of -86 ± 2 mV at pH 4.5 was measured. Since the ζ-potential of the NPs prior to reaction with THOPS was only -43 ± 2 mV, addition of THOPS was deemed successful. This batch of particles was labelled SS100-THOPS-1.

3.3.3 Secondary Functionalization of Silica NPs

With the THOPS-stabilized NP suspension prepared, we could begin to study the effect of reaction pH without risking particle aggregation. For each pH value to be tested (pH 1, 4, and 7), 12.5 mL of SS100-THOPS-1 was added to 100 mL of the respective pH solution. Each solution was brought to 74 °C. Once the reaction temperatures stabilized at 74 degrees, 1 mL of THOPS neutralized with 2.35 mL of 1 M KOH was added to each reactor dropwise. The reactions were run for 6 hours. After the reactions were finished, the pH of each of the solutions was tested. It was confirmed that the pH values did not deviate from their initial values during the course of the reaction, as was expected by the control experiment. The particles were washed by centrifugation, re-dispersed in a total of 12.5 mL of nanopure water, and stored over ion exchange resin. Particles submitted to a second round of functionalization were labelled SS100-THOPS-2-pH-1, SS100-THOPS-2-pH-4, and SS100-THOPS-2-pH-7.

3.3.4 Evaluation of the Hydrolytic Stability of Grafted THOPS

All batches of silica particles were stored in nanopure water over ion exchange resin after functionalization. However, it is known that functionalized silica particles in the presence of water can degrade over time due to hydrolysis of the covalent linkage between the grafted molecule and the NP surface.[58–61] Refer back to Section 1.2.5 for the discussion about the hydrolysis of silanes. The concern is that due to hydrolysis, all functionalized particles, independent of reaction pH, might reach an equilibrium grafting density of THOPS. If this were true, then even if the reaction pH has an immediate influence on the grafting density, prolonged exposure to water might counteract that initial increase. Since ζ-potential and conductometric titration measurements were conducted after the particles were stored for a week, hydrolysis may have enough time to interfere.

First, we tested the hydrolytic stability of a batch of 100nm THOPS-functionalized silica NPs (NC100-THOPS) stored over ion exchange resin in pH 4.5 water over the course of five months. For this experiment, we simply recorded the ζ-potential at the beginning and end of the five-month period. Next, we wanted to determine if an acidic storage environment could accelerate the hydrolysis of grafted THOPS. To answer the question, we took aliquots of NC100-THOPS and re-suspended them in pH 1 solution, pH 4.5 water, or pH 7 solution. The pH 1 and 7 solutions were taken from the same stock solutions used for the agglomeration control experiments. After one week of storage, the particles were washed three times with nanopure water, re-suspended in pH 4.5 water, and stored over ion exchange resin overnight before the measurement of ζ-potentials.

3.4 Results

Grafting densities for SS100-THOPS-1, SS100-THOPS-2-pH-1, SS100-THOPS-2-pH-4, and SS100-THOPS-2-pH-7 were quantified one week after storage over ion exchange resin via conductometric titration and ζ-potential.[6,13,22] Other methods used in the literature to quantify grafting density include elemental analysis,[62] potentiometric titration,[31] and titra-

tion with phenolphthalein indicator.[31] Another commonly cited characterization method for quantifying grafting densities on a silica surface is thermogravimetric analysis (TGA).[29–31] We also explored using TGA as a grafting density quantification method, but it was ultimately abandoned for this purpose due to conflicting results with ζ-potential and titration data. However, we did end up using TGA to obtain accurate and precise NP weight percents needed for interpretation of conductometric titration data. See Appendix C for the use of TGA to obtain accurate weight percents.

3.4.1 Zeta-Potential

A Malvern Zetasizer Nano ZS90 was used to obtain ζ-potentials according to the Smoluchowski model. Before the first round of THOPS functionalization, the SS100 particles showed a ζ-potential of -43.1 ± 1.5 mV at pH 4.5. This value increased in magnitude to -86.10 ± 1.65 mV after the first functionalization step with THOPS, indicating the successful grafting of many THOPS molecules. However, the ζ-potential was only slightly enhanced after the second THOPS addition, and it was completely independent of reaction pH, as is shown in Figure 15. Note that in this figure, ζ-potentials increase in magnitude *downward*.

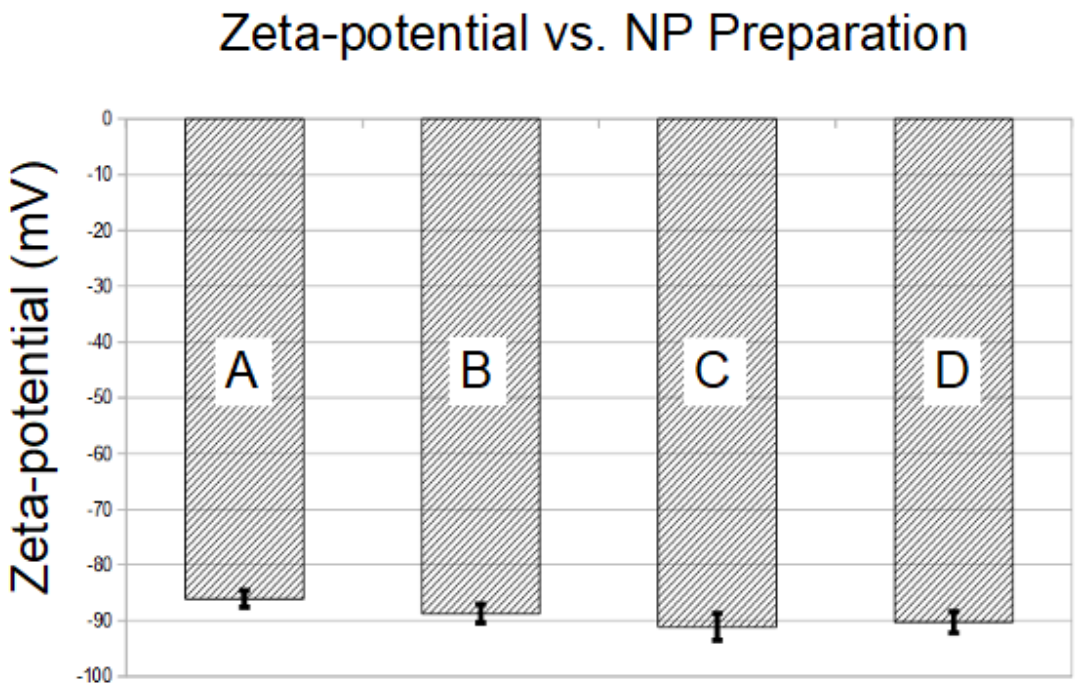

Figure 15: ζ-potentials of particles before and after functionalization. A: SS100-THOPS-1, B: SS100-THOPS-2-pH-1, C: SS100-THOPS-2-pH-4, D: SS100-THOPS-2-pH-7.

3.4.2 Conductometric Titration

Conductometric titration was also used to determine the average surface charge for each NP sample. In a typical trial, 300 µL of sample was added to 27.5 mL of 50 µM KCl solution inside a 50-mL polypropylene centrifuge tube. A conductivity probe (Hanna HI5522) was immersed in the KCl solution and kept at the same height for each trial. The reason for using KCl rather than DI water is explained in Appendix D. A 0.5 cm stir bar was spun at maximum speed to keep the solution well-mixed. The titrant (9.92×10^{-4} M KOH) was added in 50 µL aliqouts. The equivalence point was determined by taking the minimum value of the curve and averaging three trials for each sample.

From the volume of titrant used to reach the equivalence point, we calculated the total number of protons in the solution. We assume that the only source of protons in solution

Table 3: Grafting densities and charge densities by conductometric titration

Sample	Grafting density (THOPS nm^{-2})	Charge density ($\mu C\,cm^{-2}$)
SS100-THOPS-1	0.18 ± 0.01	2.9 ± 0.2
SS100-THOPS-2-pH-1	0.25 ± 0.03	4.0 ± 0.5
SS100-THOPS-2-pH-4	0.23 ± 0.05	3.7 ± 0.8
SS100-THOPS-2-pH-7	0.19 ± 0.01	3.0 ± 0.2

were due to grafted THOPS molecules. Thus, knowing the weight percent of the suspension allows the calculation of the number of strong acid groups per unit mass of the NPs. To convert to grafting densities and surface charges, we used the SSA of SS100 particles supplied by the manufacturer, which was 45 $m^2\,g^{-1}$.

Conductometric titration tells the same story as the ζ-potential measurements. The results of the conductometric titration are summarized in Table 3. Although a slight increase in the surface charge (grafting density) was seen after a second addition of THOPS, there is no significant pH-dependence on the amount of grafted THOPS.

3.4.3 Hydrolytic Stability

Figure 16 shows how storage duration and conditions affected the ζ-potential of NC100-THOPS particles. (Note that ζ-potentials increase in magnitude *downward*.) Between October 2020 and March 2021, a period of five months, the ζ-potential increased in magnitude from -75 ± 2 mV to -84 ± 1 mV. Since hydrolysis of THOPS molecules would lead to a ζ-potential smaller in magnitude, this change cannot be explained by hydrolysis over time. Instead, it is quite likely that the THOPS molecules were hydrolytically stable and that this 9 mV increase was due to the presence of ion exchange resin. Over time, the resin decreases the concentration of ions in solution, which can screen negative charges on the NP surface. Similar enhancements in ζ-potentials due to ion exchange resin have been reported in the literature.[63] Also shown in Figure 16 is the dependence of ζ-potential on storage pH. Even

in a pH 1 environment, which would be the most likely pH to catalyze hydrolysis reactions, no significant difference is seen in the ζ-potential compared with usual storage at pH 4.5. Based on both of these results, we conclude that one week of storage is not enough time for hydrolysis to alter the grafting density of THOPS-functionalized NPs.

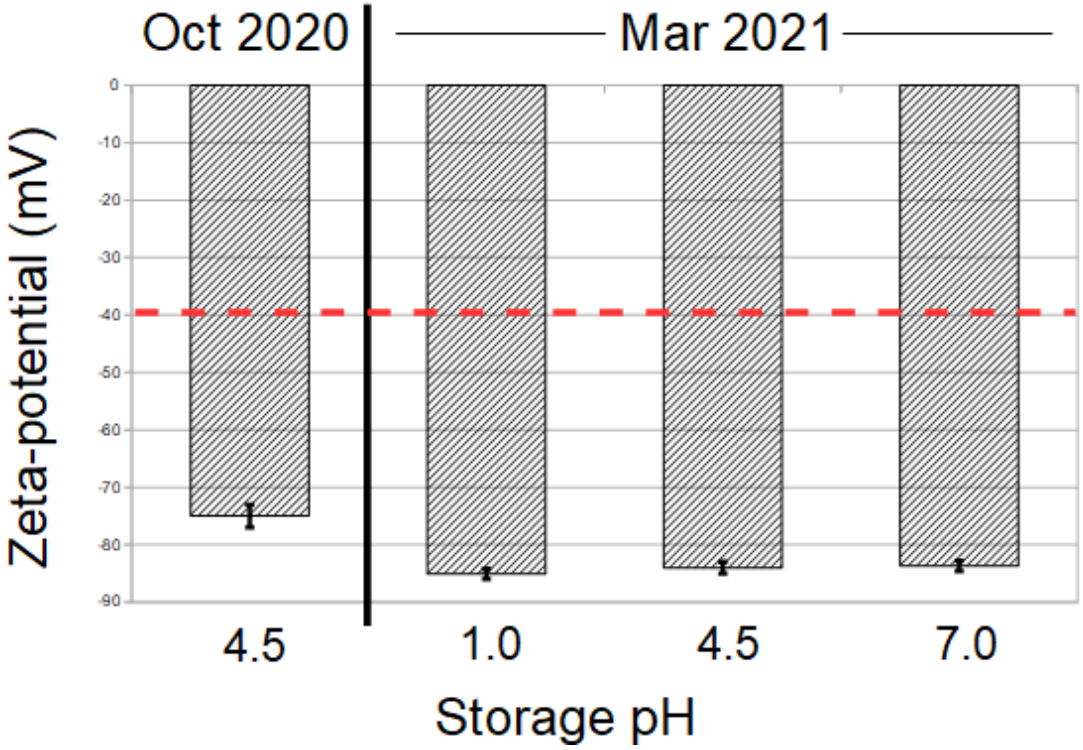

Figure 16: ζ-potentials for 100 nm THOPS-functionalized silica NPs as a function of storage duration and pH. The red horizontal dashed line represents the baseline ζ-potential of silica NPs before surface modification with THOPS. No loss of NP functionality is witnessed over five months of storage in pH 4.5 water over ion exchange resin. Storage for one week in various pH environments also has no detrimental effect on the NP ζ-potential.

3.5 Discussion

Conductometric titration and ζ-potential measurements both show that although there was a slight increase in the grafting density after a second addition of THOPS, this increase did not depend upon the pH of the reaction. Moreover, because THOPS exhibits high levels

of hydrolytic stability, we have ruled out possible interference from post-reaction hydrolysis. Thus, two questions remain. First, why did pH not influence the grafting density? Second, what is a promising, alternate path towards increasing the surface charge of silica NPs using THOPS? In the next few sections, this first question is addressed. Two hypotheses are presented, and experiments are suggested to test these hypotheses. The second question is addressed in the concluding chapter of this thesis.

3.5.1 First Hypothesis: Unfavorable Electrostatic Interactions

In many cases, electrostatic interactions between molecules on the surface of silica NPs are great enough to cause drastic changes in the system. For example, in one study, electrostatic repulsion between drugs bound to a NP surface and surface silanols caused the drugs to be released.[64] In another study,[65] it was shown that unfavorable electrostatic interactions between neighboring carboxylate groups caused the average pKa of these groups to increase by two pH units (see Figure 17). Unlike carboxylic acid ligands, THOPS is a strong acid with pKa < 1,[22] which implies that it stays ionized even in low pH environments. Thus, the total number of unfavorable electrostatic interactions between THOPS molecules increases without recourse as more THOPS molecules are grafted onto a silica NP. One hypothesis, then, for the failure of pH to influence the grafting density of THOPS is that electrostatic repulsion between grafted THOPS molecules imposes a limit on the grafting density, as is illustrated in Figure 18.

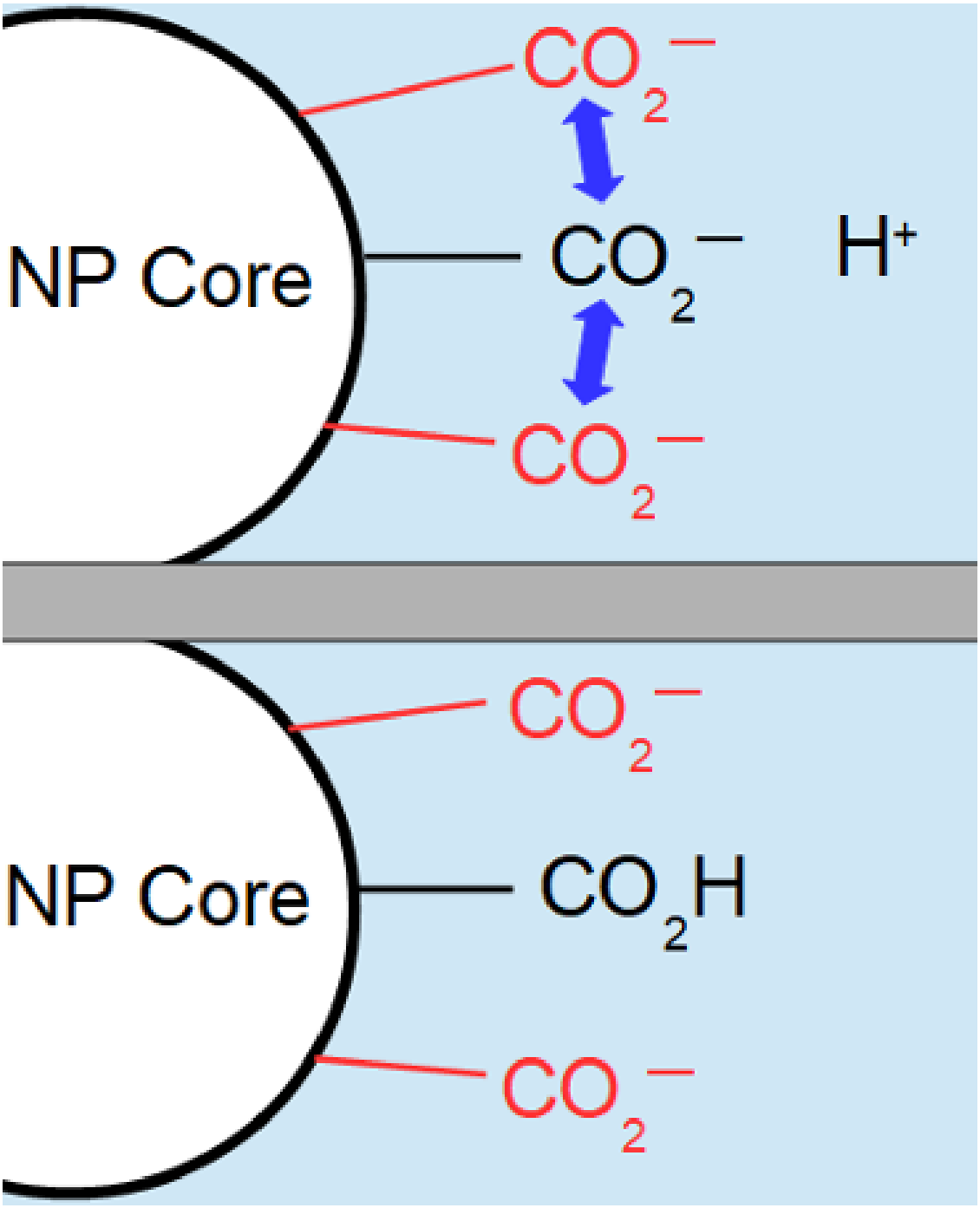

Figure 17: It is known that unfavorable electrostatic repulsion between neighboring carboxylate groups (top) can be eliminated via an in increase in the average pKa of the carboxylate groups (bottom).

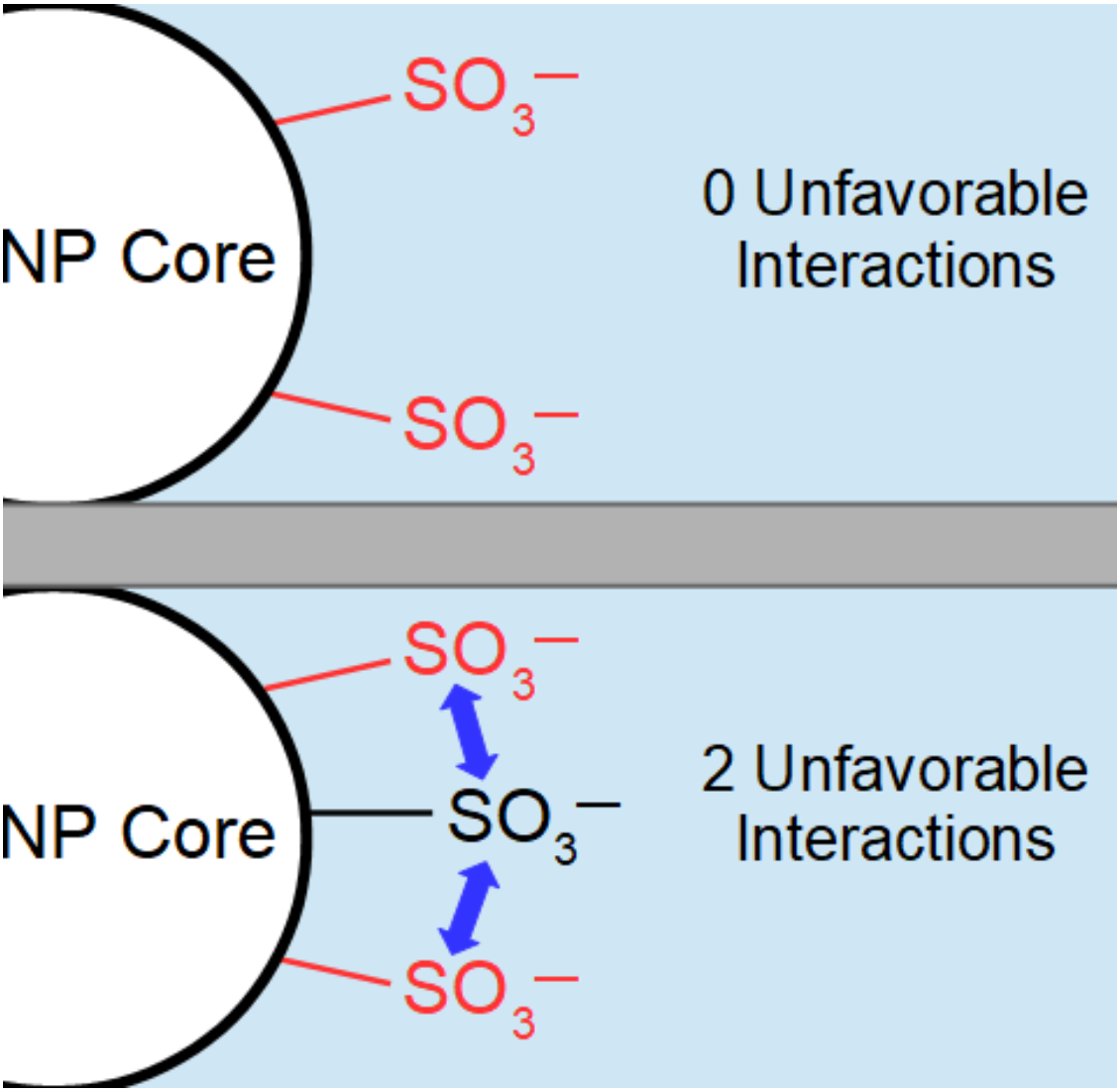

Figure 18: The number of unfavorable electrostatic interactions between THOPS molecules increases as more THOPS is grafted onto a silica NP surface. Top: the grafting density of THOPS is small enough for no unfavorable electrostatic interactions to exist. Bottom: the grafting density of THOPS is large enough so that unfavorable electrostatic interactions are unavoidable.

To test this hypothesis, a THOPS functionalization reaction could be run in aqueous solutions of different ionic strengths. The prediction is that reactions run in solutions with higher ionic strength would lead to NPs with higher grafting densities due to the screening of charge by the ions present. After the experiment is run, if higher ionic strengths correlate with higher grafting densities, then it is likely that electrostatic interactions indeed limit

the grafting density of THOPS. We would then adjust our functionalization procedure to include the addition of optimal amounts of ions for the purpose of screening. The hydrolytic stability of these NPs would have to be tested over time, because hydrolysis may be more favorable now that surface groups are more dense and are forced to interact unfavorably. If, on the other hand, no change in grafting density results from varying the ionic strength of the reaction, then electrostatic interactions are not a limiting factor for grafting. This negative result would suggest a different, second hypothesis, which is given in the next section.

3.5.2 Second Hypothesis: Crowding

A second hypothesis is that physical crowding of THOPS molecules on the NP surface, not electrostatic repulsion, is the main obstacle to achieving high grafting densities. The density of silanols on a typical silica NP surface is 4.9 OH/nm^2.[29,34] This value already imposes a hard limit for the maximum grafting density of THOPS, because THOPS must condense with surface silanols for grafting to occur. However, this maximum value is practically impossible to attain when grafting bulky molecules such as THOPS. Brinker and Scherer found that the grafting density of hydrocarbon chains on silica NPs decreases with increasing chain size. They attribute this trend to physical crowding (see Figure 19).[34] It is possible that in our system, after a critical grafting density of THOPS is reached, the NP surfaces become so saturated so as to prevent the grafting of any more THOPS (Figure 20). Since THOPS has a similar size to the ligand O-$(CH_2)_4$, a theoretical maximum grafting density of about 3 THOPS nm^{-2} is not unreasonable based on Brinker and Scherer's finding. Moreover, it has been reported that in a silica surface modification using a certain trialkoxysilane, only 50% of the available silanols were consumed due to steric hindrance of the added groups.[66] Half of the available silanols equates to about 2.5 THOPS nm^{-2}, which is close to a value of 3.

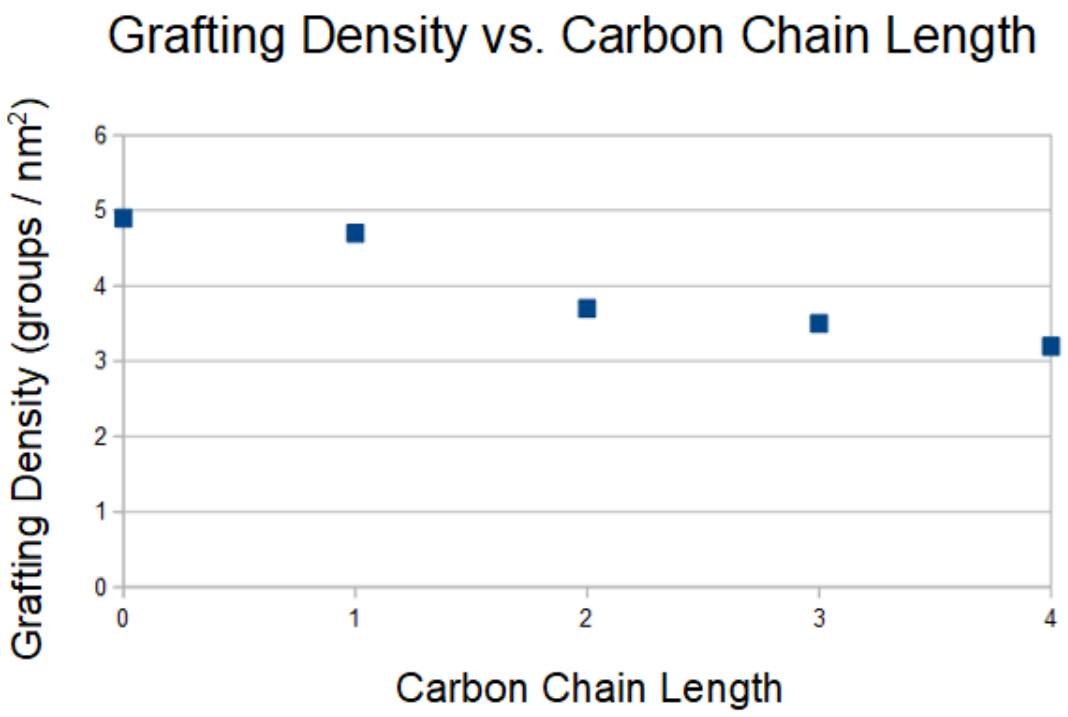

Figure 19: Grafting densities as a function of carbon chain length n for electrically neutral ligands HO-$(CH_2)_n$. As n increases, the grafting density decreases.

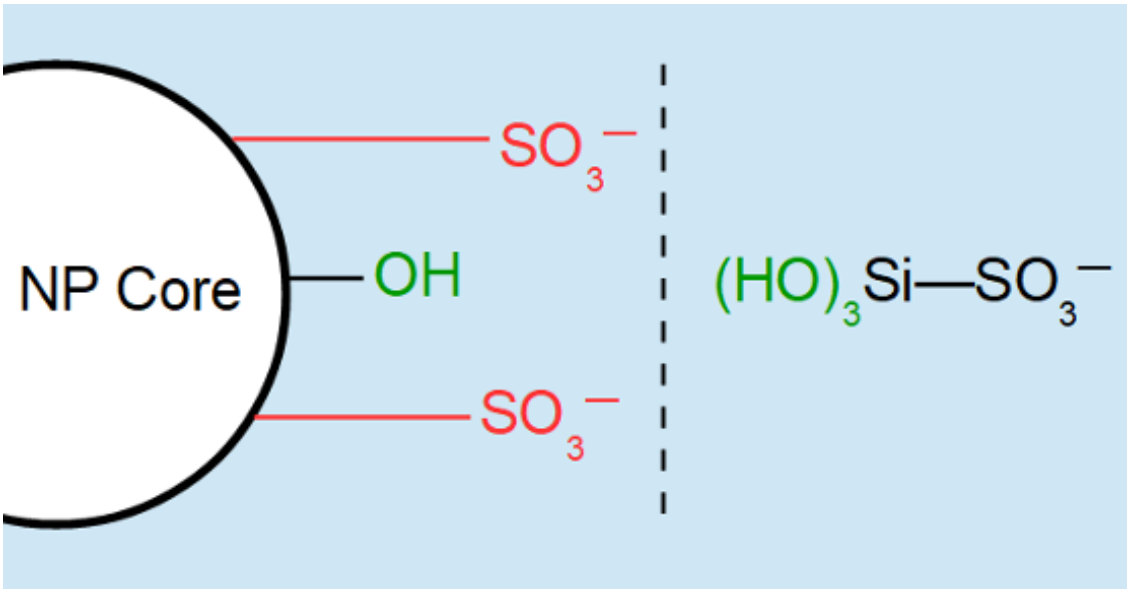

Figure 20: After a critical number of THOPS molecules (shown in red) are attached to the NP surface, steric repulsion makes further silanol coupling reactions between THOPS and silanols on the NP surface energetically unfavorable (silanols shown in green).

Assuming that the first hypothesis has already been tested and no correlation has been found between the grafting density of THOPS and solvent ionic strength, it may not be necessary to test the crowding hypothesis. No other hypothesis seems very likely for explaining why there is a limit to the grafting density of THOPS which is independent of pH. Indeed, the very fact that a second addition of THOPS led to only a marginal increase in the surface charge for all pH values may be enough evidence to conclude that crowding is the most likely obstacle we are facing. More, due to the finite surface area available on each NP, physical crowding may not be easily overcome. In the concluding chapter, an alternate approach is suggested which could circumvent the crowding issue.

4.0 Conclusion and Future Work

In the second chapter of this thesis, the development and use of a RZC protocol to significantly increase the monodispersity of silica NPs was demonstrated. The application of this protocol to isolating monodisperse particles of $\leq$ 50 nm diameters for use in CCAs is possible as long as centrifuges with higher rotor speeds are available. CCAs built from more monodisperse particles would exhibit fewer ordering defects, which would lead to higher diffraction efficiencies and narrower stopbands.

In the third chapter of this thesis, the synthesis of highly charged silica NPs using THOPS was demonstrated, but there was a limit to the grafting density which was independent of reaction pH. At the moment, we are unsure whether this limit is due primarily to electrostatics, physical crowding, or possibly a combination of both. If the main obstacle to grafting density is physical crowding, then an obvious solution would be to explore the use of NPs which have larger surface areas. Mesoporous NPs (MNPs) are NPs with extensive three-dimensional internal pore structures. Due to their large surface areas and open channels, they are perfect for imparting functionality with high-density.[63,67] Moreover, it is possible to synthesize monodisperse, 40 nm MNPs for use as PhC devices.[63] Thus, it would be very interesting to compare the surface charge of THOPS-functionalized MNPs to the surface charge of the NPs we have been using.

The entirety of this thesis, then, points forward to future for which the probability of improving DUV-diffracting CCAs is great. An idealized workflow is summarized in Figure 21. First, the contribution of electrostatics in limiting grafting density will be determined. It may turn out that higher grafting densities can be achieved by the screening of electrostatic interactions. On the other hand, if screening of charge does not aid in increasing the grafting density, then MNPs will be investigated as a new substrate for the grafting of THOPS. MNPs promise higher grafting densities due to their larger surface area. Thus, by one method or another, THOPS-functionalized silica NPs of very large surface charge will be synthesized. The next step would then be to isolate monodisperse fractions of these highly-charged silica NPs by RZC. Finally, DUV-diffracting CCAs using the obtained highly-charged, monodis-

perse silica NPs will be fabricated. We expect great improvements in the quality of these CCAs from those previously reported in our group.[6]

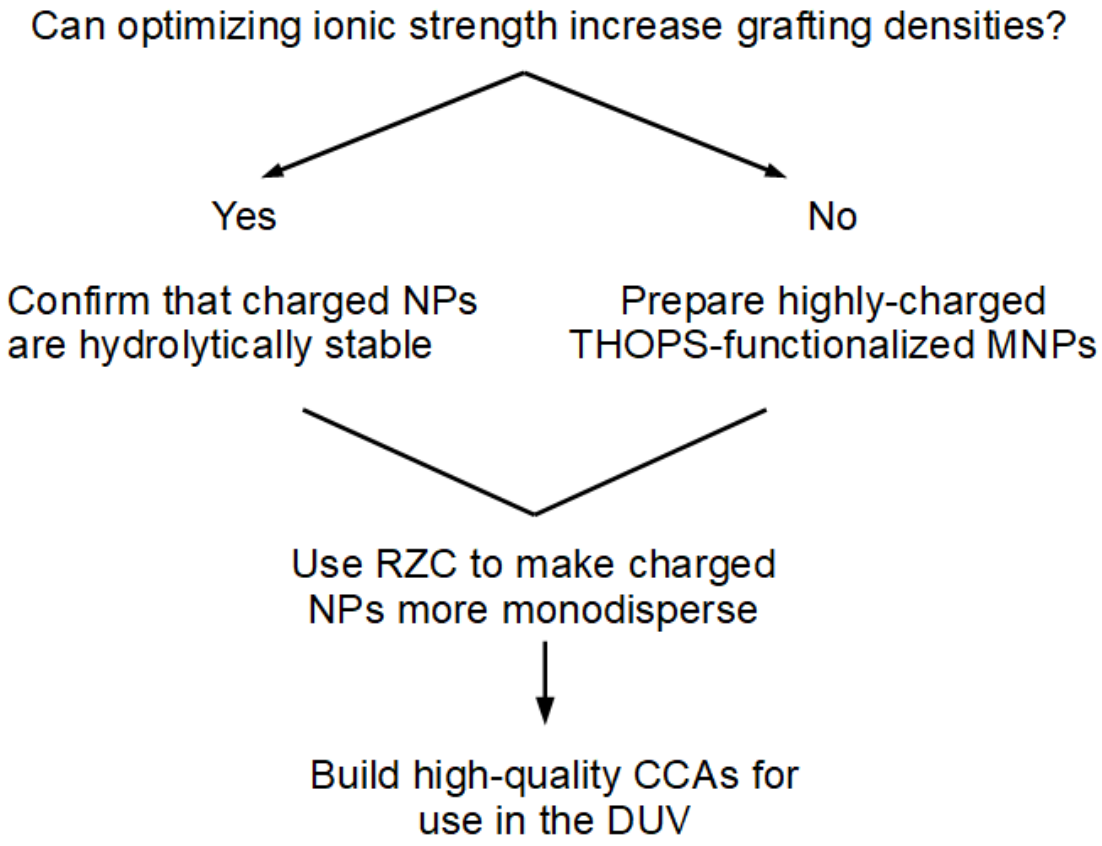

Figure 21: Flowchart outlining a future work plan for developing DUV-diffraction CCAs.

Appendix A Transmission Electron Micrographs

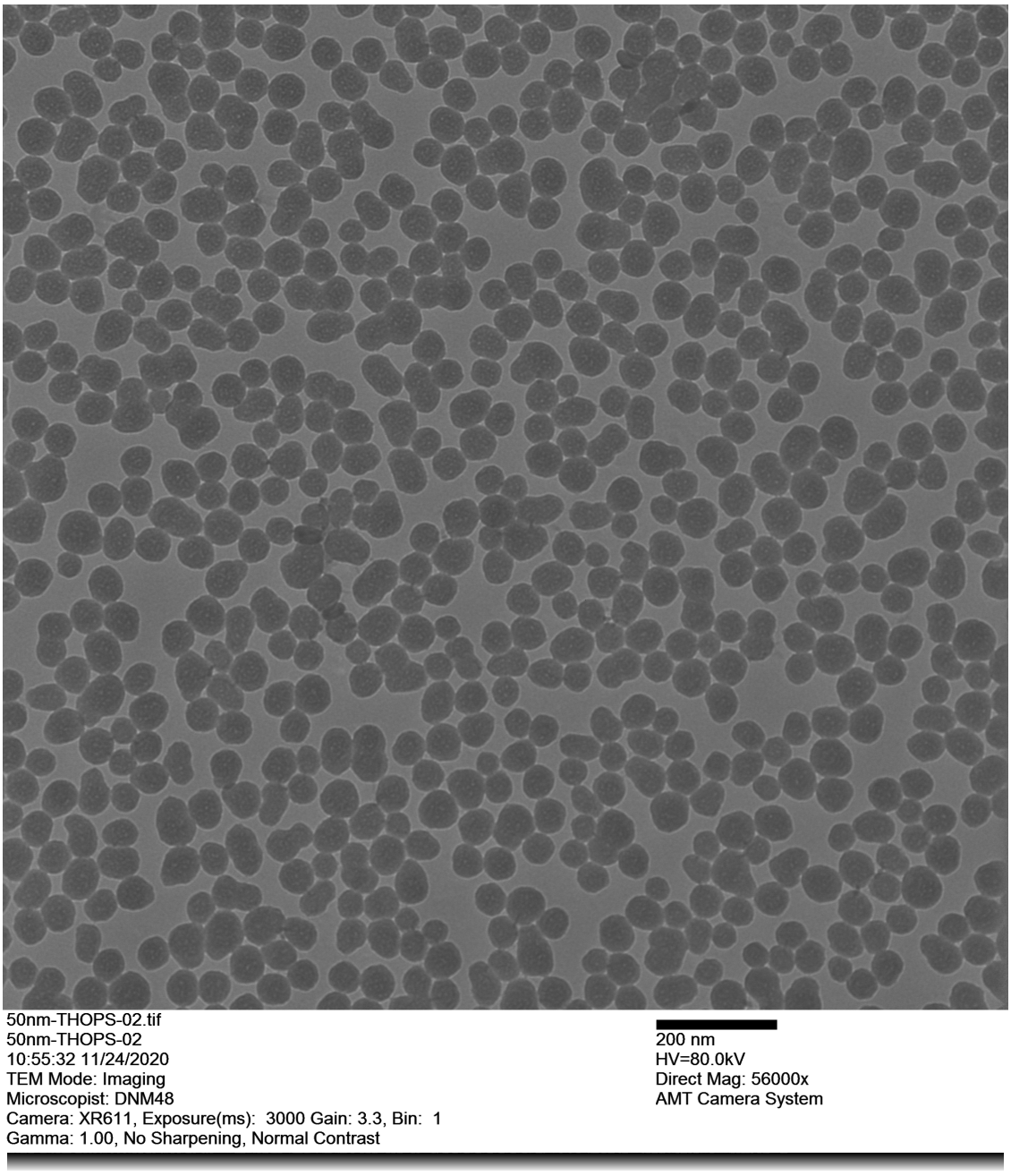

Figure 22: TEM of 50 nm THOPS-functionalized silica NPs. As is shown here, THOPS-functionalization can lead to particles which have decreased size monodispersity and which are less perfectly spherical than non-functionalized particles.

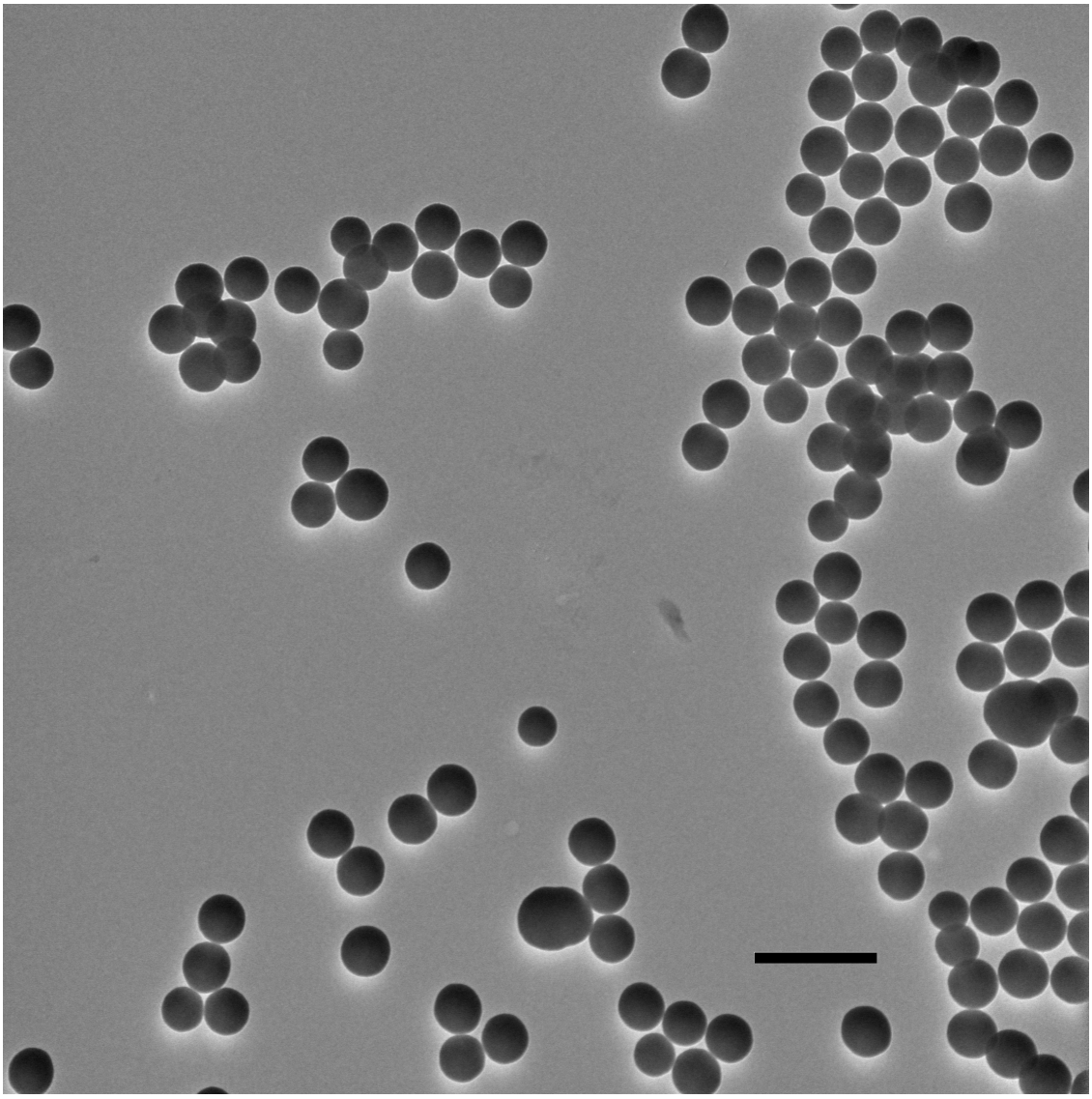

Figure 23: TEM of 185 nm silica NPs before RZC. The scale bar represents a distance of 500 nm.

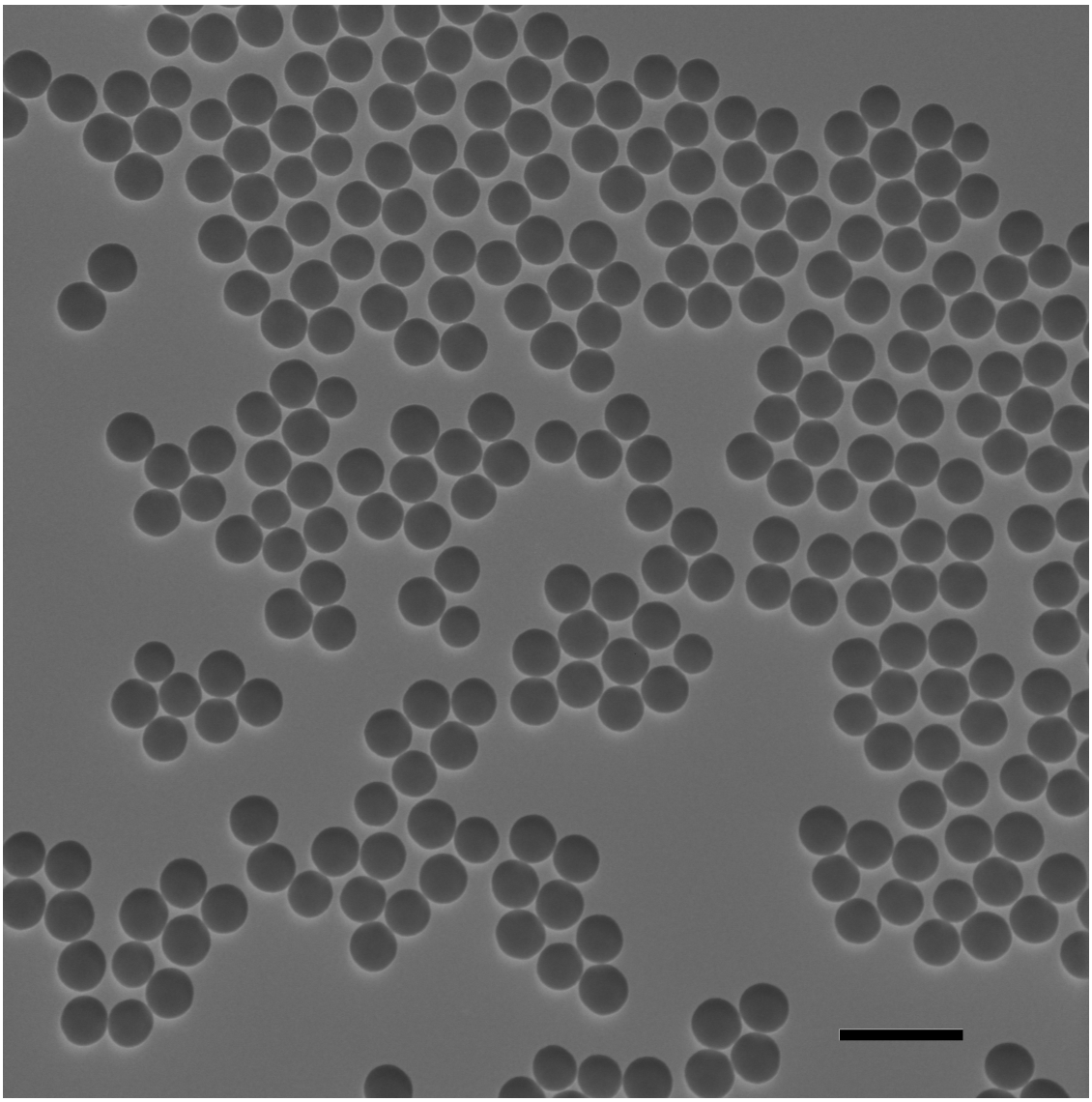

Figure 24: TEM of 185 nm silica NPs after RZC. The scale bar represents a distance of 500 nm.

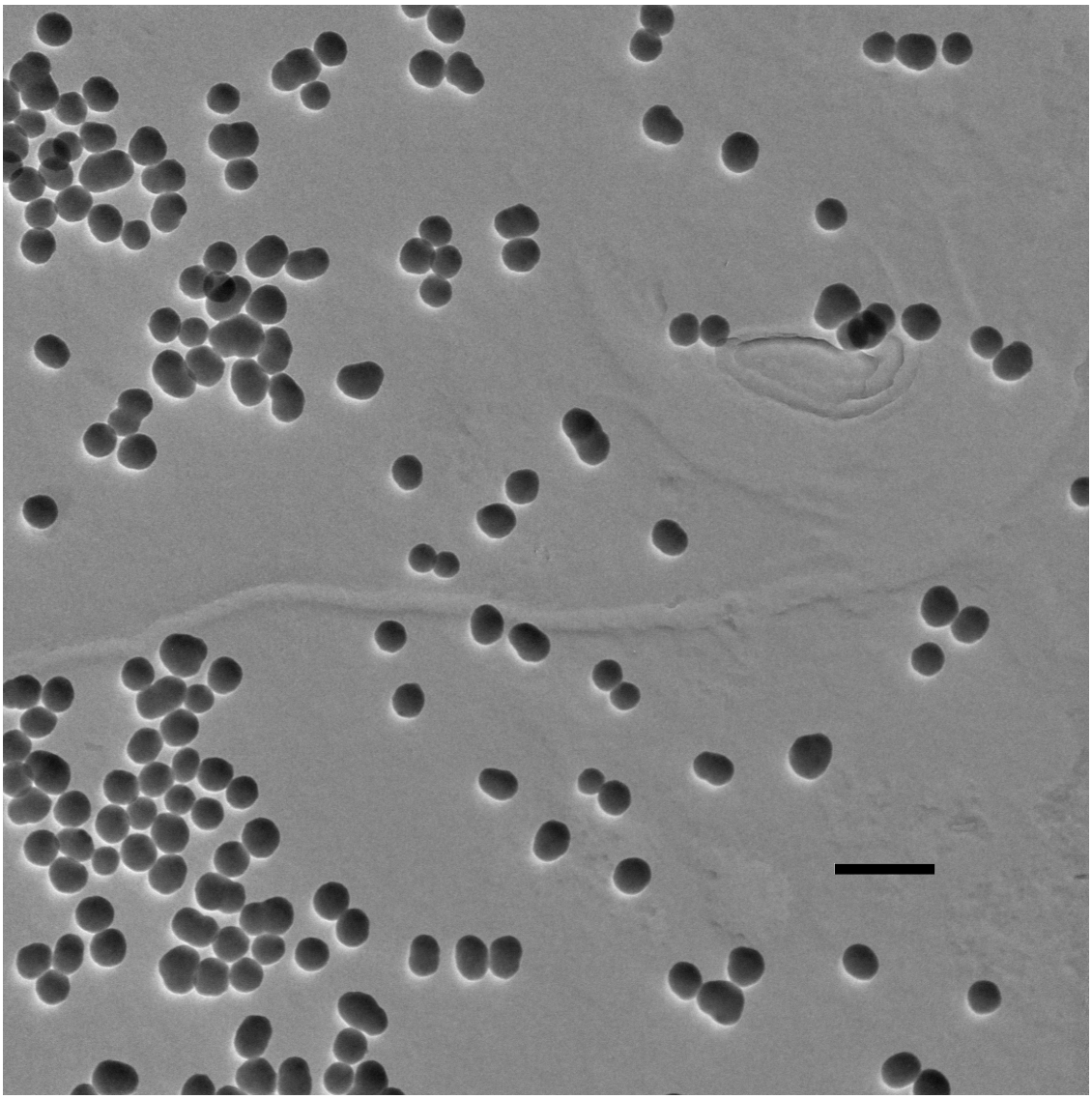

Figure 25: TEM of SS100. The scale bar represents a distance of 200 nm.

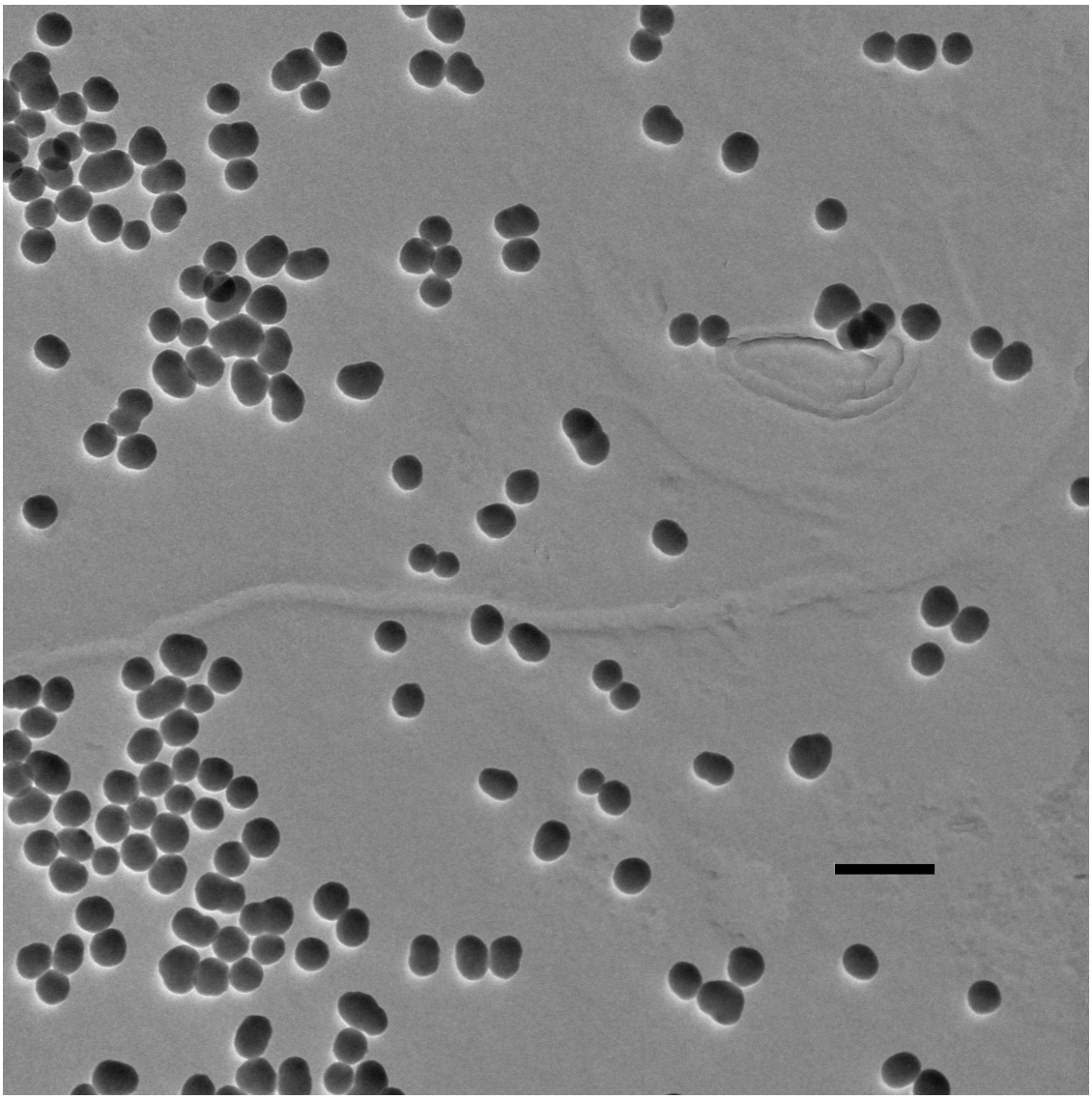

Figure 26: TEM of SS100-THOPS-1. The scale bar represents a distance of 200 nm.

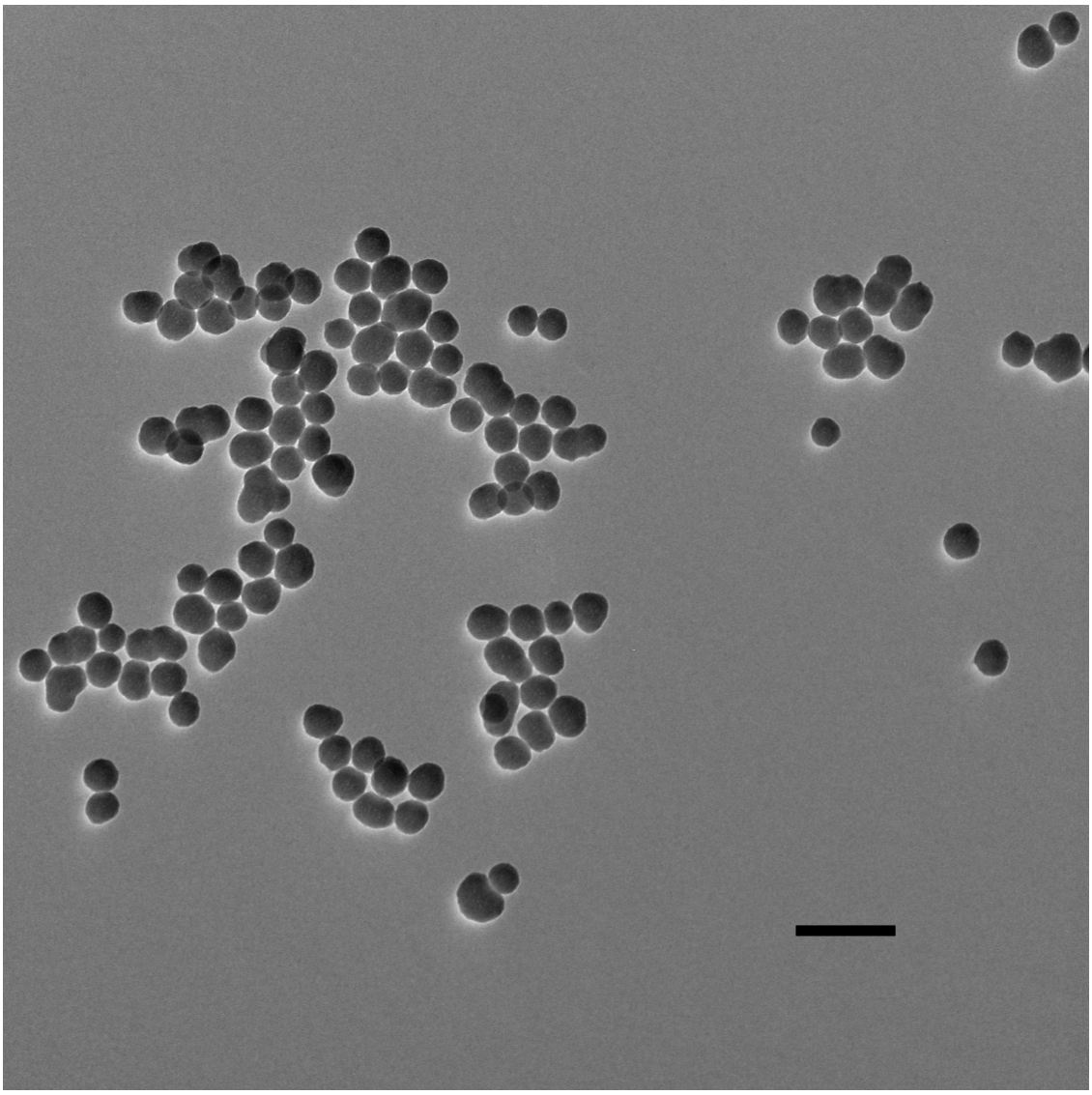

Figure 27: TEM of SS100-THOPS-2-pH-1. The scale bar represents a distance of 200 nm.

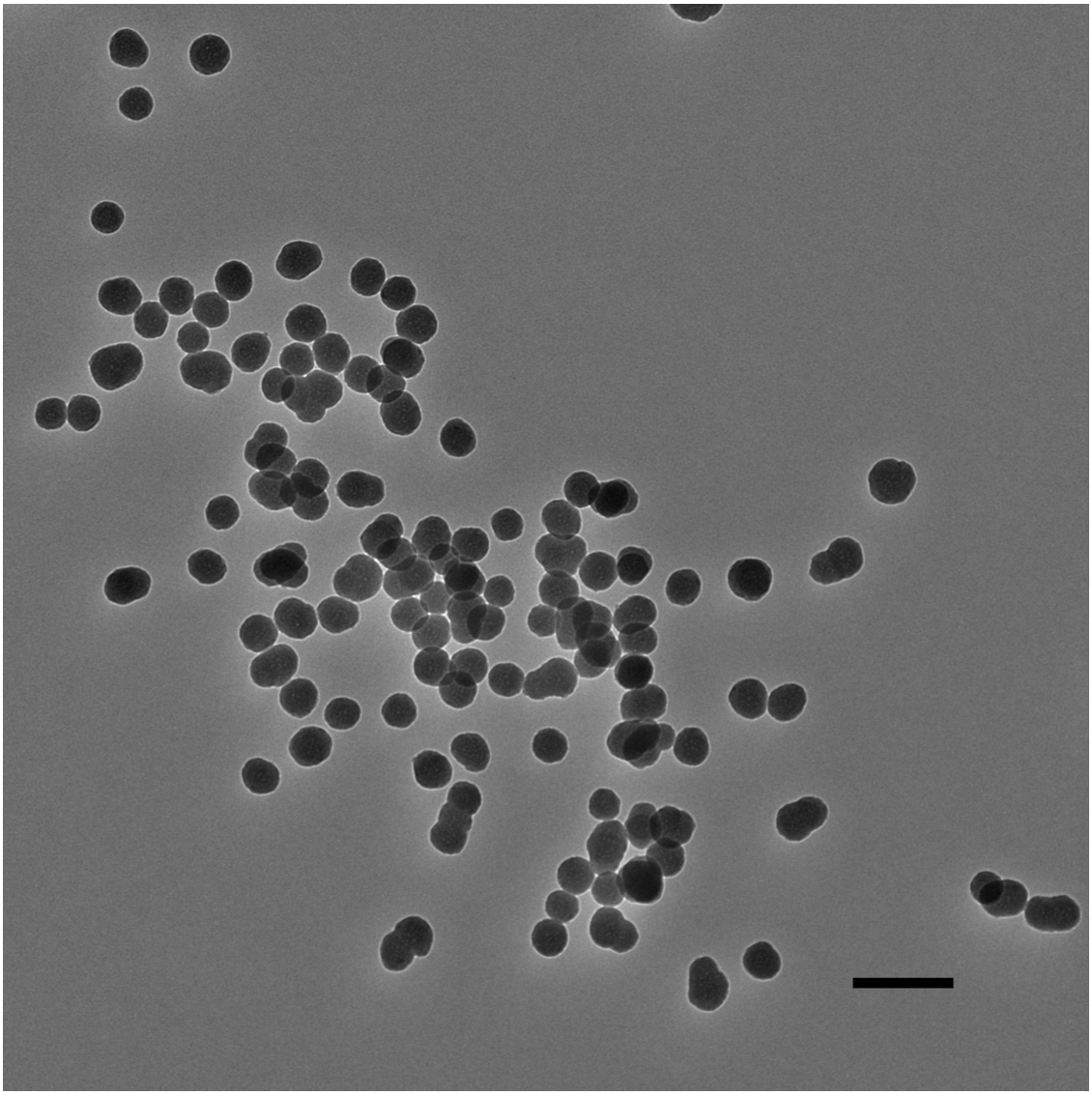

Figure 28: TEM of SS100-THOPS-2-pH-4. The scale bar represents a distance of 200 nm.

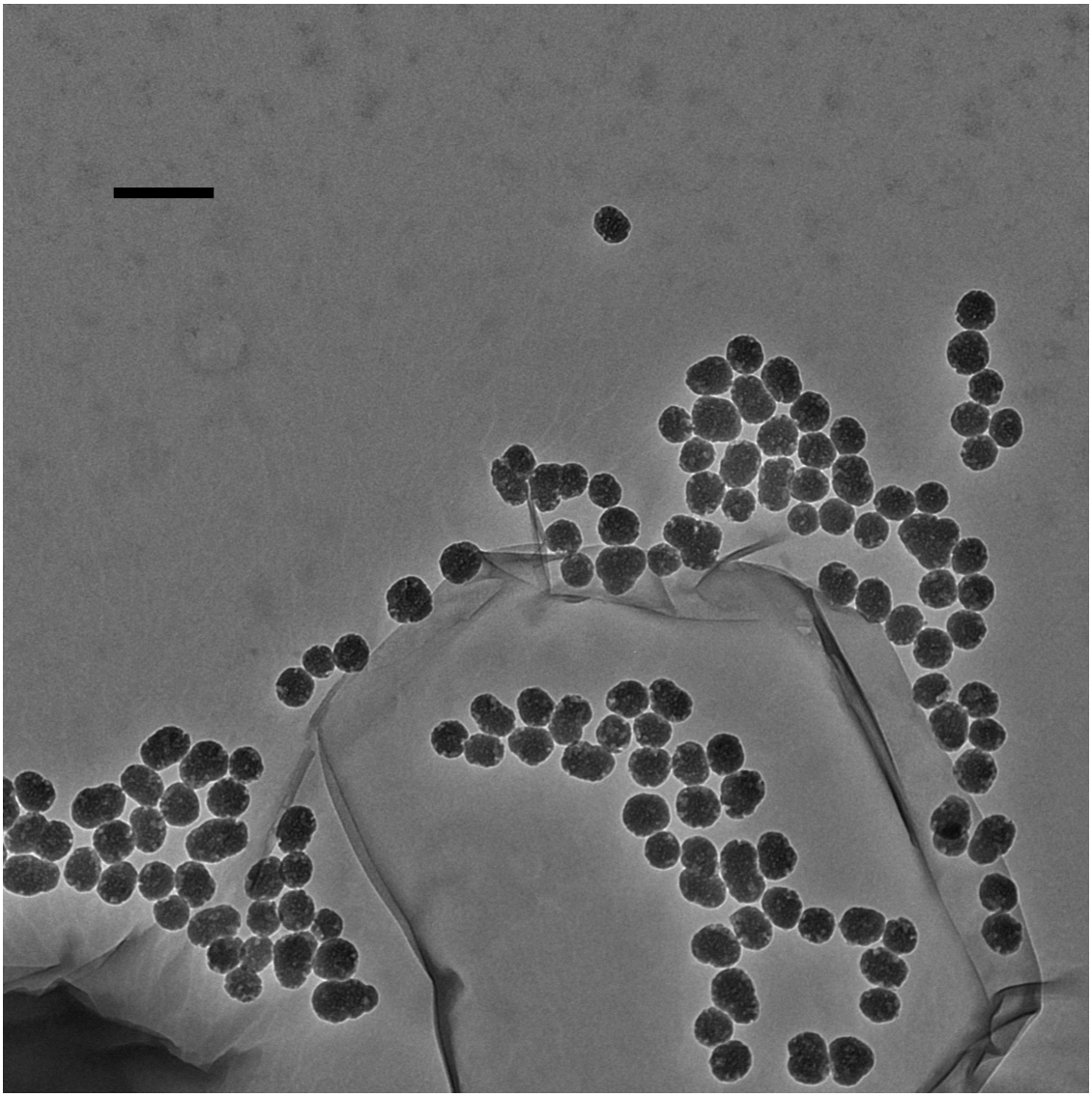

Figure 29: TEM of SS100-THOPS-2-pH-7. The scale bar represents a distance of 200 nm.

Appendix B RZC Calculations and Plots

Parameters were calculated in the following manner. The sucrose gradient density $\rho(h)$ was calculated by converting from sucrose concentration to density at 25 °C using a table.[68] The minimum and maximum density values used in the gradient were 1.12 and 1.24 $\mathrm{g\,mL^{-1}}$. Experimental silica NP densities are higher and range from 1.87 to 1.95 $\mathrm{g\,mL^{-1}}$.[69–71] In this study, an intermediate value of $\rho_p = 1.9$ was taken to be the NP density. The viscosity $\eta(h)$ also varies with sucrose concentration; these values were found by interpolating table entries from a beet sugar handbook.[72] The rotor speed of 3200 RPM was used as the angular velocity ω. Finally, the hydrodynamic diameter d of the 185 nm NPs was taken to be 215 nm, the same as measured by DLS.

To plot h as a function of time, a few intermediate mathematical steps had to be done, since Equation 7 makes no reference to a time variable. First, the time to a given displacement value h was calculated by integrating the reciprocal of the sedimentation velocity, via:

$$t(h) = \int_0^h \frac{1}{v(x)}\,dx \tag{8}$$

Next, this function was inverted to find h in terms of t. Figure 12 compares the values calculated via this procedure to the observed displacements. Excellent agreement between theory and experiment validates the hypothesis that the upper layer contained the 185 nm unagglomerated particles. A similar plot was generated for THOPS-functionalized 100 nm silica NPs (Figure 30). In this case, the theoretical sedimentation rate overestimated the experimental rate. Since functionalized NPs bear large amounts of surface charge, this observed difference between theory and experiment could be due to the fact that Equation 7 does not take into account electrostatic interactions between particles.

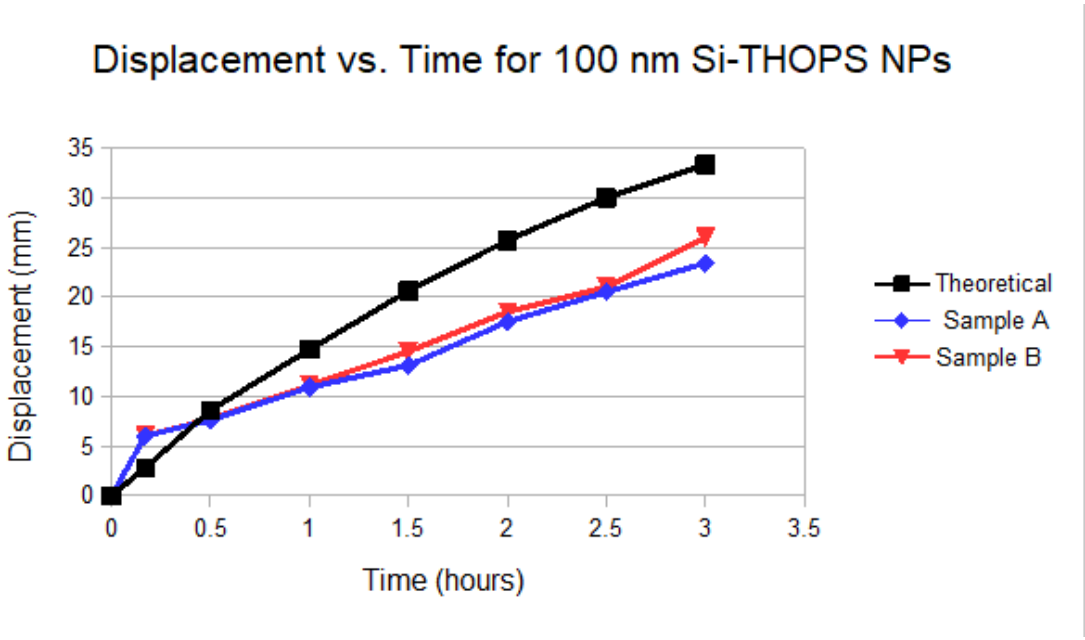

Figure 30: Sedimentation of NC100-THOPS NPs at 3200 RPM (rcf = 1334 × g at the top of the centrifuge tube). Instrument: Sorvall TC7 centrifuge equipped with a swinging bucket rotor (RTH-250); Chamber Temperature: 25°C; Density gradient steps: 250, 350, 400, 510, 600 mg/mL sucrose, top to bottom, step heights: 0.91, 0.94, 0.99, 1.0, and 1.05 cm, respectively.

Appendix C Determination of Weight Percents

The weight percent (w/v) of a nanoparticle suspension is the ratio of nanoparticle mass to total volume of the suspension. Using this terminology, a NP suspension with a concentration of 1 gram silica per 100 mL of suspension is expressed as 1 wt%. In theory, measuring the weight percent is a simple task. By adding a known volume of well-mixed NP suspension to a tared glass vial and dehydrating the sample in an oven, the combined mass of the vial and NP suspension can be recorded and used to calculate the weight percent. Performing multiple trials presumably increases the certainty of the measurement. However, a flaw was noticed in this standard approach, which was the error due to water adsorption. During the sample's trip between oven and balance, some water vapor from the lab air is adsorbed both onto the glass vial and onto the dehydrated silica itself. (Silica is very hygroscopic and is in fact used as a desiccant.[73,74]) To prove that water adsorption occurs, a glass vial was placed in an oven at 80 °C for twenty minutes. Then, the vial was quickly transferred to a balance across the lab and its mass was measured over time. Figure 31 shows that the vial gains mass over time due to water adsorption. Therefore, unless extra steps are taken to account for water adsorption, accurate weight percents cannot be obtained using this method. Moreover, since the lab humidity varies from day to day, some sort of calibration would have to be done every time weight percents are to be measured.

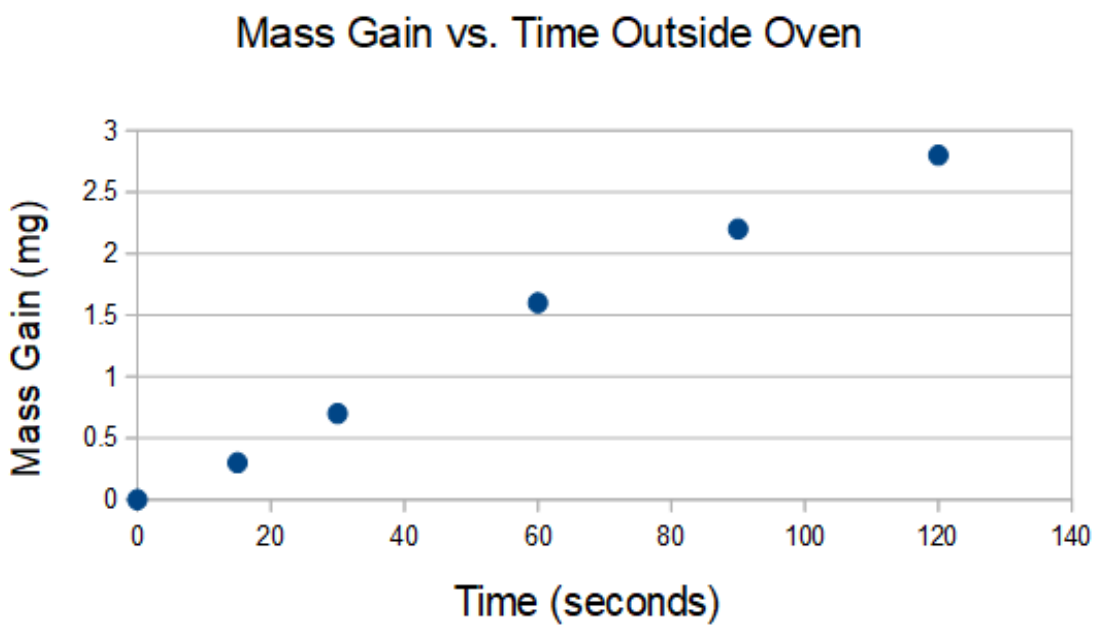

Figure 31: Mass gain of vial-silica NP system over time due to water adsorption.

TGA provides a solution to this water adsorption problem. Since a TGA instrument is, simply put, a furnace equipped with an analytical balance, the NP suspension mass can be monitored directly during dehydration, eliminating the trip through the moist air. Weight percents were measured as follows. First, an empty TGA pan was inserted into the TGA instrument (Perkin Elmer STA 6000), held at 90 °C for 10 minutes, heated to 200 °C at a ramp rate of 40 °C/min, and held at temperature for another 10 minutes. This provided a background signal for the weight percent experiments. N_2 gas was used to purge the headspace at a flow rate of 20 mL/min. Next, 50.0 µL of each NP suspension was added to a TGA pan and subjected to the same thermal treatment as the empty pan. A typical TGA curve is shown in Figure 32. The NP mass for each trial was taken to be the average value of the baseline-subtracted mass from 120 °C onward. The average value and standard deviation of the weight percent for each sample was determined from three trials each.

Table 4: Weight percents of SS100-THOPS-1 and SS100-THOPS-2 particles as determined by TGA

Sample	Weight Percent (g / 100 mL)
SS100-THOPS-1	2.66 ± 0.12
SS100-THOPS-2-pH-1	5.23 ± 0.10
SS100-THOPS-2-pH-4	4.63 ± 0.15
SS100-THOPS-2-pH-7	4.04 ± 0.07

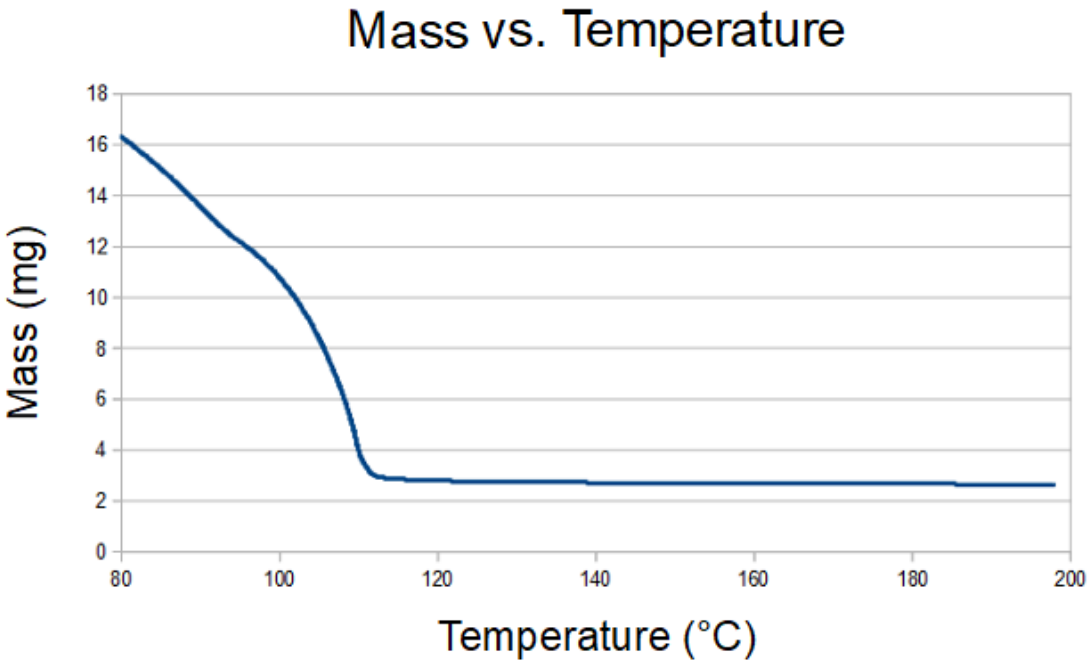

Figure 32: Example TGA curve showing the mass loss of a silica NP suspension over time. Water is driven off from 80 °C to 110 °C. The residual mass is due to silica.

Using the TGA data and taking into account the uncertainty in pipette volume, weight percents with uncertainties were calculated for each NP suspension (data summarized in Table 4).

Appendix D The Role of KCl in a Conductometric Titration

The reactions involved in a conductometric titration are ion exchange and acid-base neutralization (shown below).

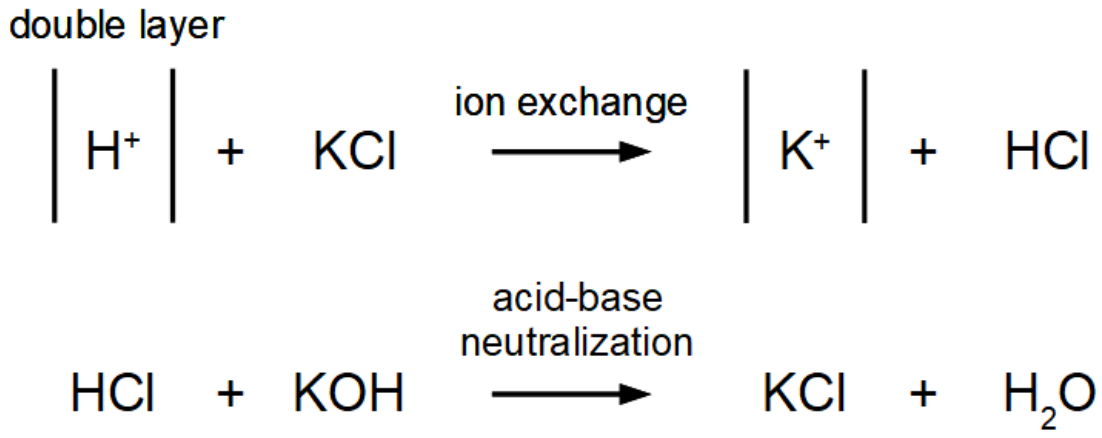

In the first step, KCl acts an an ion exchange agent.[31,33] Protons dissociated from grafted THOPS molecules of a given NP can become trapped inside the electric double layer surrounding it. Adding KCl produces K^+ ions which displace trapped protons through ion exchange. Since the conductivity of H^+ is greater than that of K^+, the result is an enhancement in the sensitivity of the titration experiment. Thus, addition of the background electrolyte KCl leads to more accurate determination of the equivalence point in the second step, which is the acid-base neutralization reaction.[75]

Bibliography

[1] Moore, D. S. *Sensing and Imaging: An International Journal* **2007**, *8*, 9–38.

[2] Gares, K. L.; Bykov, S. V.; Asher, S. A. *The Journal of Physical Chemistry A* **2017**, *121*, 7889–7894.

[3] Wallin, S.; Pettersson, A.; Östmark, H.; Hobro, A. *Analytical and Bioanalytical Chemistry* **2009**, *395*, 259–274.

[4] Zrimsek, A. B.; Bykov, S. V.; Asher, S. A. *Applied Spectroscopy* **2019**, *73*, 601–609.

[5] Lopez-Moreno, C.; Palanco, S.; Laserna, J. J.; DeLucia Jr, F.; Miziolek, A. W.; Rose, J.; Walters, R. A.; Whitehouse, A. I. *Journal of Analytical Atomic Spectrometry* **2006**, *21*, 55–60.

[6] Hufziger, K. T.; Bykov, S. V.; Asher, S. A. *Applied Spectroscopy* **2017**, *71*, 173–185.

[7] Heimann, P. A.; Urstadt, R. *Applied Optics* **1990**, *29*, 495–501.

[8] Shur, M. S.; Gaska, R. *IEEE Transactions on Electron Devices* **2009**, *57*, 12–25.

[9] Myers, A. B.; Mathies, R. A. *Biological Applications of Raman Spectroscopy* **1987**, *2*, 1–58.

[10] Asher, S. A. *Annu. Rev. Phys. Chem* **1988**, *39*, 537–588.

[11] Tuschel, D. D.; Mikhonin, A. V.; Lemoff, B. E.; Asher, S. A. *Applied Spectroscopy* **2010**, *64*, 425–432.

[12] Cooper, J. K.; Grant, C. D.; Zhang, J. Z. *The Journal Of Physical Chemistry A* **2013**, *117*, 6043–6051.

[13] Hufziger, K. T.; Bykov, S. V.; Asher, S. A. *Applied Spectroscopy* **2014**, *68*, 1219–1223.

[14] Hufziger, K. T.; Zrimsek, A. B.; Asher, S. A. *ACS Applied Nano Materials* **2018**, *1*, 7016–7024.

[15] Shimmin, R. G.; DiMauro, A. J.; Braun, P. V. *Langmuir* **2006**, *22*, 6507–6513.

[16] Kaplan, C. N.; Wu, N.; Mandre, S.; Aizenberg, J.; Mahadevan, L. *Physics of Fluids* **2015**, *27*, 092105.

[17] Kwon, S.-H.; Park, H.-G.; Lee, Y.-H. *Semiconductors and Semimetals*; Elsevier, 2012; Vol. 86; pp 301–333.

[18] Pan, G.; Tse, A. S.; Kesavamoorthy, R.; Asher, S. A. *Journal of the American Chemical Society* **1998**, *120*, 6518–6524.

[19] Asher, S. A.; Weissman, J. M.; Tikhonov, A.; Coalson, R. D.; Kesavamoorthy, R. *Physical Review E* **2004**, *69*, 066619.

[20] Bohn, J. J.; Ben-Moshe, M.; Tikhonov, A.; Qu, D.; Lamont, D. N.; Asher, S. A. *Journal of Colloid and Interface Science* **2010**, *344*, 298–307.

[21] De Graef, M.; McHenry, M. E. *Structure of Materials: An Introduction to Crystallography, Diffraction and Symmetry*; Cambridge University Press, 2012.

[22] Wang, L.; Tikhonov, A.; Asher, S. A. *Applied Spectroscopy* **2012**, *66*, 426–431.

[23] Zachariasen, W. H., et al. **1945**,

[24] Hufziger, K. T. The Development of Photonic Crystal Optics and Wide-field Raman Imaging Spectrometers for Trace Explosive Detection. Ph.D. thesis, University of Pittsburgh, 2019.

[25] Li, T.; Zhou, C.; Jiang, M. *Polymer Bulletin* **1991**, *25*, 211–216.

[26] Gierada, M.; De Proft, F.; Sulpizi, M.; Tielens, F. *The Journal of Physical Chemistry C* **2019**, *123*, 17343–17352.

[27] Dugas, V.; Chevalier, Y. *Journal of Colloid and Interface Science* **2003**, *264*, 354–361.

[28] Belton, D. J.; Deschaume, O.; Perry, C. C. *The FEBS journal* **2012**, *279*, 1710–1720.

[29] Estephan, Z. G.; Jaber, J. A.; Schlenoff, J. B. *Langmuir* **2010**, *26*, 16884–16889.

[30] Park, J. T.; Seo, J. A.; Ahn, S. H.; Kim, J. H.; Kang, S. W. *Journal of Industrial and Engineering Chemistry* **2010**, *16*, 517–522.

[31] Yang, L.; Wang, Y.; Luo, G.; Dai, Y. *Microporous and Mesoporous Materials* **2005**, *84*, 275–282.

[32] Rodriguez, R.; Herrera, R.; Archer, L. A.; Giannelis, E. P. *Advanced Materials* **2008**, *20*, 4353–4358.

[33] Margolese, D.; Melero, J.; Christiansen, S.; Chmelka, B.; Stucky, G. *Chemistry of Materials* **2000**, *12*, 2448–2459.

[34] Brinker, C. J.; Scherer, G. W. *Sol-gel Science: The Physics and Chemistry of Sol-Gel Processing*; Academic press, 2013.

[35] Arkles, B.; Steinmetz, J.; Zazyczny, J.; Zolotnitsky, M. *Proceedings of the 46th Annual Reinforced Plastics/Composites Institute, Society of Plastic Industry (SPI), Washington, DC* **1991**,

[36] He, W.; Wu, D.; Li, J.; Zhang, K.; Xiang, Y.; Long, L.; Qin, S.; Yu, J.; Zhang, Q. *Bulletin of the Korean Chemical Society* **2013**, *34*, 2747–2752.

[37] Rostamzadeh, P.; Mirabedini, S. M.; Esfandeh, M. *Journal of Coatings Technology and Research* **2014**, *11*, 651–660.

[38] Simon, A.; Cohen-Bouhacina, T.; Porté, M.; Aimé, J.; Baquey, C. *Journal of Colloid and Interface Science* **2002**, *251*, 278–283.

[39] Feichtenschlager, B.; Lomoschitz, C. J.; Kickelbick, G. *Journal of Colloid and Interface Science* **2011**, *360*, 15–25.

[40] Hu, C.; Chen, Y. *Chemical Engineering Journal* **2015**, *271*, 128–134.

[41] Perez-Potti, A.; Lopez, H.; Pelaz, B.; Abdelmonem, A.; Soliman, M. G.; Schoen, I.; Kelly, P. M.; Dawson, K. A.; Parak, W. J.; Krpetic, Z., et al. *Scientific Reports* **2021**, *11*, 1–12.

[42] Fritsch, A. *Preparative Density Gradient Centrifugations*; Beckman, 1975.

[43] Stöber, W.; Fink, A.; Bohn, E. *Journal of Colloid and Interface Science* **1968**, *26*, 62–69.

[44] Kim, S.-D.; Surabhi, S.; Choi, J.; Jeong, J.-R. *Electronic Materials Letters* **2019**, *15*, 673–679.

[45] Hartlen, K. D.; Athanasopoulos, A. P.; Kitaev, V. *Langmuir* **2008**, *24*, 1714–1720.

[46] DanieláLilly, G., et al. *Journal of Materials Chemistry* **2009**, *19*, 1390–1394.

[47] Sarmphim, P.; Jantaratana, P.; Sirisathitkul, C. *Journal of Nanomaterials* **2018**, *2018*.

[48] Bonaccorso, F.; Zerbetto, M.; Ferrari, A. C.; Amendola, V. *The Journal of Physical Chemistry C* **2013**, *117*, 13217–13229.

[49] Wong, S.; Kitaev, V.; Ozin, G. A. *Journal of the American Chemical Society* **2003**, *125*, 15589–15598.

[50] Anderson, N. G., et al. *Natl Cancer Inst Monogr* **1966**, *21*, 9–39.

[51] Hiemenz, P. C.; Rajagopalan, R. *Principles of Colloid and Surface Chemistry, Revised and Expanded*; CRC press, 2016.

[52] Castañeda, M.; Sánchez, R.; Santiago, R. *Analytical Biochemistry* **1971**, *44*, 381–387.

[53] Walter, J.; Lohr, K.; Karabudak, E.; Reis, W.; Mikhael, J.; Peukert, W.; Wohlleben, W.; Colfen, H. *ACS nano* **2014**, *8*, 8871–8886.

[54] Nishiyama, N.; Shick, R.; Ishida, H. *Journal of Colloid and Interface Science* **1991**, *143*, 146–156.

[55] Manzano, J. S.; Wang, H.; Kobayashi, T.; Naik, P.; Lai, K. C.; Evans, J. W.; Slowing, I. I. *Microporous and Mesoporous Materials* **2020**, *305*, 110276.

[56] Pirez, C.; Lee, A.; Manayil, J.; Parlett, C.; Wilson, K. *Green Chemistry* **2014**, *16*, 4506–4509.

[57] de ON Ribeiro, J.; Nunes, E. H.; Vasconcelos, D. C.; Vasconcelos, W. L.; Nascimento, J. F.; Grava, W. M.; Derks, P. W. *Journal of Porous Materials* **2019**, *26*, 1581–1591.

[58] Ossenkamp, G. C.; Kemmitt, T.; Johnston, J. H. *Chemistry of Materials* **2001**, *13*, 3975–3980.

[59] O'Gara, J. E.; Alden, B. A.; Gendreau, C. A.; Iraneta, P. C.; Walter, T. H. *Journal of Chromatography A* **2000**, *893*, 245–251.

[60] Borges, E. M. *Journal of Chromatographic Science* **2015**, *53*, 580–597.

[61] Borges, E. M.; Volmer, D. A. *Journal of Chromatographic Science* **2015**, *53*, 1107–1122.

[62] Zheng, F.-C.; Chen, Q.-W.; Hu, L.; Yan, N.; Kong, X.-K. *Dalton Transactions* **2014**, *43*, 1220–1227.

[63] Yamamoto, E.; Kitahara, M.; Tsumura, T.; Kuroda, K. *Chemistry of Materials* **2014**, *26*, 2927–2933.

[64] Lee, C.-H.; Lo, L.-W.; Mou, C.-Y.; Yang, C.-S. *Advanced Functional Materials* **2008**, *18*, 3283–3292.

[65] Wang, D.; Nap, R. J.; Lagzi, I.; Kowalczyk, B.; Han, S.; Grzybowski, B. A.; Szleifer, I. *Journal of the American Chemical Society* **2011**, *133*, 2192–2197.

[66] Borges, E. M. *Journal of Chromatographic Science* **2015**, *53*, 580–597.

[67] Luo, L.; Liang, Y.; Erichsen, E. S.; Anwander, R. *Journal of Colloid and Interface Science* **2017**, *495*, 84–93.

[68] Heidcamp, W. H. Cell Biology Laboratory Manual. Biology Department, Gustavus Adolphus College.

[69] Kimoto, S.; Dick, W. D.; Hunt, B.; Szymanski, W. W.; McMurry, P. H.; Roberts, D. L.; Pui, D. Y. *Aerosol Science and Technology* **2017**, *51*, 936–945.

[70] Barahona, F.; Geiss, O.; Urban, P.; Ojea-Jimenez, I.; Gilliland, D.; Barrero-Moreno, J. *Analytical Chemistry* **2015**, *87*, 3039–3047.

[71] Parnell, S.; Washington, A.; Parnell, A.; Walsh, A.; Dalgliesh, R.; Li, F.; Hamilton, W.; Prevost, S.; Fairclough, J.; Pynn, R. *Soft Matter* **2016**, *12*, 4709–4714.

[72] Asadi, M. *Beet-sugar handbook*; John Wiley & Sons, 2005; p 795.

[73] Tran, H.; Roddick, F.; O'Donnell, J. *Water Research* **1999**, *33*, 2992–3000.

[74] Jia, C.; Dai, Y.; Wu, J.; Wang, R. *Energy Conversion and Management* **2006**, *47*, 2523–2534.

[75] Labib, M. E.; Robertson, A. A. *Journal of Colloid and Interface science* **1980**, *77*, 151–161.